

# Evaluation of microseismic motion at the KAGRA site based on ocean wave data

S.Hoshino<sup>1</sup>, Y.Fujikawa<sup>1</sup>, M.Ohkawa<sup>1</sup>, T.Washimi<sup>2</sup>, and T.Yokozawa<sup>3</sup>

<sup>1</sup>*Faculty of Engineering, Niigata University, 8050 Ikarashi-2-no-cho,  
Nishi-ku, Niigata City, Niigata 950-2181, Japan*

*\*E-mail: f22c036a@mail.cc.niigata-u.ac.jp*

<sup>2</sup>*Faculty of Engineering, Niigata University, 8050 Ikarashi-2-no-cho,  
Nishi-ku, Niigata City, Niigata 950-2181, Japan*

<sup>3</sup>*Faculty of Engineering, Niigata University, 8050 Ikarashi-2-no-cho,  
Nishi-ku, Niigata City, Niigata 950-2181, Japan*

<sup>4</sup>*Gravitational Wave Science Project (GWSP), Kamioka branch, National  
Astronomical Observatory of Japan (NAOJ), Kamioka-cho, Hida City, Gifu  
506-1205, Japan*

*\*E-mail: tatsuki.washimi@nao.ac.jp*

<sup>5</sup>*Institute for Cosmic Ray Research (ICRR), KAGRA Observatory, The  
University of Tokyo, Kamioka-cho, Hida City, Gifu 506-1205, Japan*

.....  
The microseismic motion, ambient ground vibration caused by ocean waves, affects ground-based gravitational wave detectors. In this study, characteristics of the ocean waves including seasonal variations and correlation coefficients were investigated for the significant wave heights at 13 coasts in Japan. The relationship between the ocean waves and the microseismic motion at the KAGRA site was also evaluated. As a result, it almost succeeded in explaining the microseismic motion at the KAGRA site by the principal components of the ocean wave data. One possible application of this study is microseismic forecasting, an example of which is also presented

.....  
Subject Index      xxxx, xxx

# 1 Introduction

Gravitational waves are ripples in space-time propagating at the speed of light and their direct observation is a key probe in advanced astronomy. The first successful detection was performed in 2015 by the advanced Laser Interferometer Gravitational-Wave Observatory (LIGO, USA) [1, 2], and the first simultaneous detections by LIGO and Virgo (Italy) were performed in 2017 [3–5]. KAGRA is a laser interferometric gravitational wave detector with 3 km arms in Japan [6]. Two solo observation runs were conducted in 2015 and 2018 [7, 8], and the first international joint observation run (O3GK) with GEO 600 in Germany was conducted from April 7–21, 2020 [9, 10]. KAGRA has two unique features compared with other kilometer-scale detectors in the world: (1) it is constructed underground at Kamioka to reduce the ground vibration noise, (2) the test mass mirrors are cooled down to reduce thermal noise. To attain and maintain the working point of the detector, all mirror positions, angles, and motions must be controlled. When external disturbances occur, maintaining these controls becomes difficult, and the resonant state is broken. Consequently, the gravitational wave observations must be stopped. This state is called "lock loss" and a reduction in the lock loss rate is important for performing meaningful observations. During the O3GK period, it was occasionally difficult to keep the KAGRA interferometer in a locked state when microseismic motions, which are ground vibrations with a frequency range of about 0.1–0.5 Hz induced by ocean waves, were significant [10–12]. The mechanism of microseismic motion excited by ocean waves was derived by Longuet-Higgins [13] and approximated using a non-linear equation extended by Hasselmann [14]. This approximation was evaluated using the normal-mode equation derived by Tanimoto to obtain negligible errors for ground vibrations occurring in the ocean to a depth of approximately 1 km [15, 16]. Microseismic motion is related to the amplitude and period of the waves, with the period of the ground motions being approximately half the period of the waves, and the magnitude of the motions being derived from the energy of the waves, as shown by Bromirski *et al.* [17].

In this study, we investigate the relationship between the microseismic motion at the KAGRA site and the activity of the ocean waves around Japan; Although this relationship has been expected qualitatively, it has not been studied quantitatively. Sec. 2 explains the details of the seismometers installed at the KAGRA site and the behavior of the measured microseismic motion. In Sec. 3, the characteristics of the ocean waves around Japan are discussed based on public data. In Sec. 4, we propose an approximate equation connecting the microseismic motion at the KAGRA site to the wave height at various coasts in Japan. Finally, in Sec. 5, the results of this study are summarized and its useful application, a forecast of future microseismic motion, is shown.

## 2 Characterizations for the microseismic motion at the KAGRA site

In this section, we explain the information about the seismometers used in this study and the characteristics of their data. To monitor the environments around the KAGRA interferometer, several sensors were installed at the experimental site and continuously logged using the KAGRA DAQ system [18]. Three seismometers were placed at each end and corner station, and the horizontal axes were aligned with the orientations of the arms [19]. The seismometers used are the Trillium 120QA from *Nanometrics Inc.*, which are sensitive to ground velocity in three directions from 0.01 Hz to 10 Hz. Fig. 1 shows examples of the amplitude spectral density (ASD) of the ground velocity of these seismometers in each location and direction. In this figure, two different days are shown to compare high- and low-noise days, with black dashed lines representing Peterson’s high/low seismic noise model [20]. The significant peak at 0.1–0.5 Hz corresponding to the microseismic motion is seen in all ASDs and its amplitude and structure are almost the same in the stations and the directions for both days. The amplitude below 0.05 Hz varies in the channels, and this behavior is assumed to be due to atmospheric pressure [21, 22]. Based on these results, for simplicity, the vertical signal of the seismometer located at the corner station was used to represent ground vibration in this study.

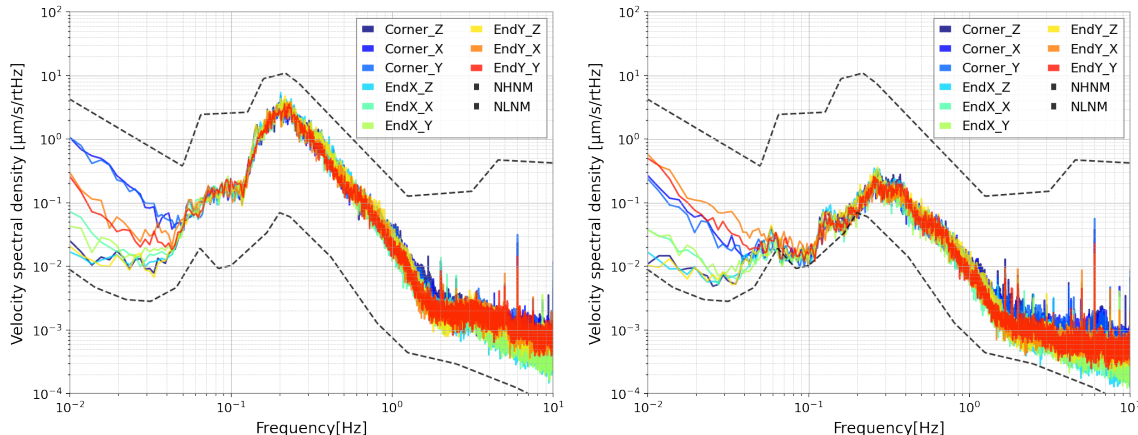


**Fig. 1** Amplitude spectral densities (ASDs) of the ground velocity, for each location (Corner, X-end, Y-end) and each direction (X, Y, Z) at the KAGRA site. The measurement time is 4096 seconds on February 18 (left) and June 10 (right) in 2020. Black dashed lines represent Peterson’s high/low seismic noise model [20].

The band-limited root mean square (BLRMS) of the seismometer signal was used to evaluate the time dependence of microseismic motion at the KAGRA site. BLRMS is the

root mean square every 20 minutes for the time series data filtered using a bandpass filter (`TimeSeries.bandpass` in `gwpy 2.1.4`) from 0.1 Hz to 0.5 Hz, to limit the frequency band. Fig. 2 shows an example from February 2020. All the data for 2020 are shown in A. In the O3GK run, the KAGRA interferometer was difficult to keep locked when the BLRMS value was above  $0.3 \mu\text{m/s}$  and was impossible to keep locked when the BLRMS value was over  $0.5 \mu\text{m/s}$  [12].

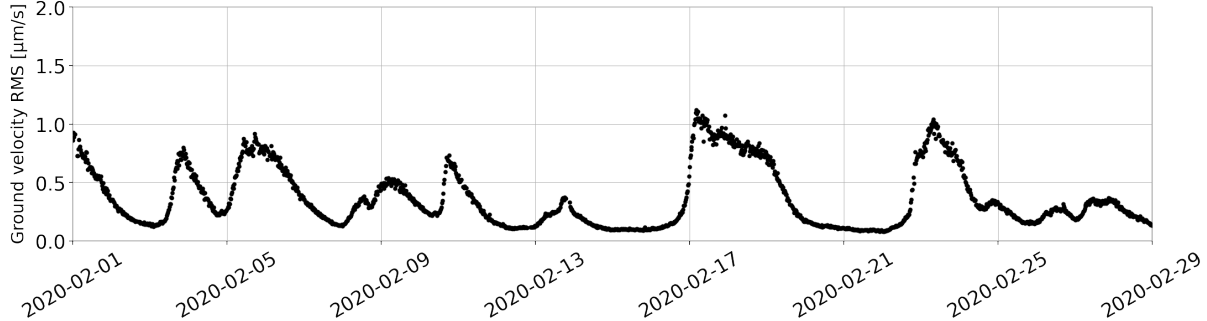


**Fig. 2** The root mean square of the microseismic motion (0.1–0.5 Hz) at the KAGRA site during February 2020. All data for 2020 are shown in the A.

Fig. 3 shows the time ratio for every week in 2020, classified by the microseismic motion level into three ranges: below  $0.3 \mu\text{m/s}$  (green), between  $0.3 \mu\text{m/s}$  and  $0.5 \mu\text{m/s}$  (yellow), and above  $0.5 \mu\text{m/s}$  (red). The microseismic motion increased from winter to the beginning of spring (December–March) and remained stable at small values in summer. It also shows large values at the beginning of autumn (September and October) owing to typhoons.

### 3 Characterizations for the ocean waves around Japan

Significant wave height (SWH,  $H_{1/3}$ ) is the average of the highest one-third (33%) of waves (measured from trough to crest) that occur in a given period [23] and is widely used as an indicator of the strength of ocean waves. Wave data are provided by *the Nationwide Ocean Wave information network for Ports and HARborS* (NOWPHAS) operated by *the Port and Harbor Bureau, Ministry of Land, Infrastructure, Transport and Tourism, Japan* [24]. NOWPHAS data are measured every 20 minutes using the zero-up-cross method [25]. Seven sites on the Sea of Japan coast (Niigata, Naoetsu, Toyama, Wajima, Fukui, Tsuruga, and Shibayama) and six sites on the Pacific side (Soma, Onahama, Kashima, Shimoda, Shimizu, and Omaesaki), as shown in Fig. 4, are selected for use in this study from the NOWPHAS data. Among the selected sites, the closest one is Toyama, about 45 km, and the farthest one

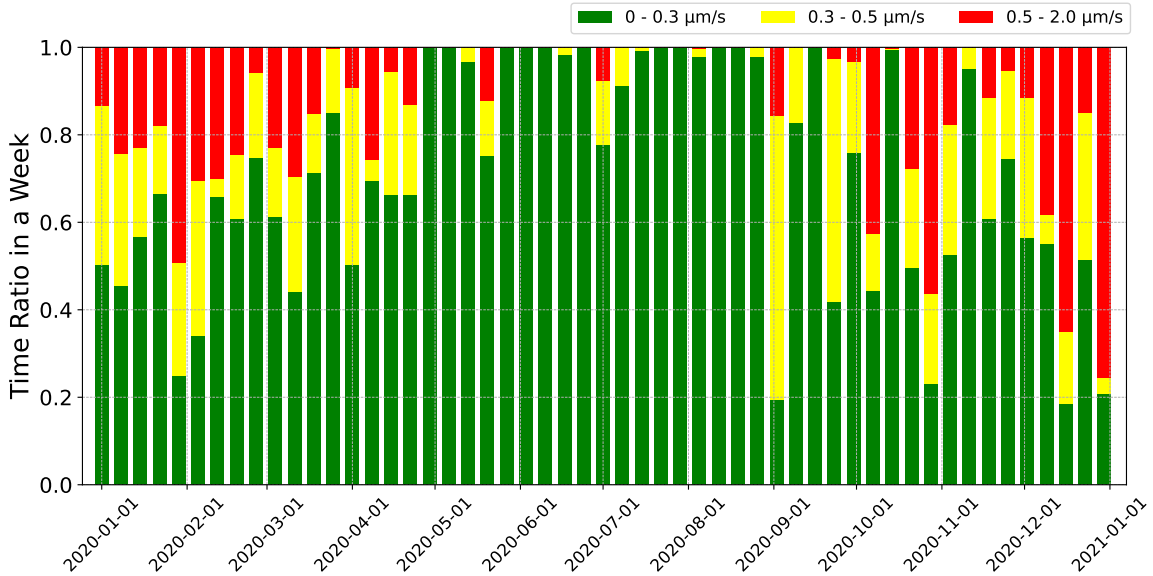
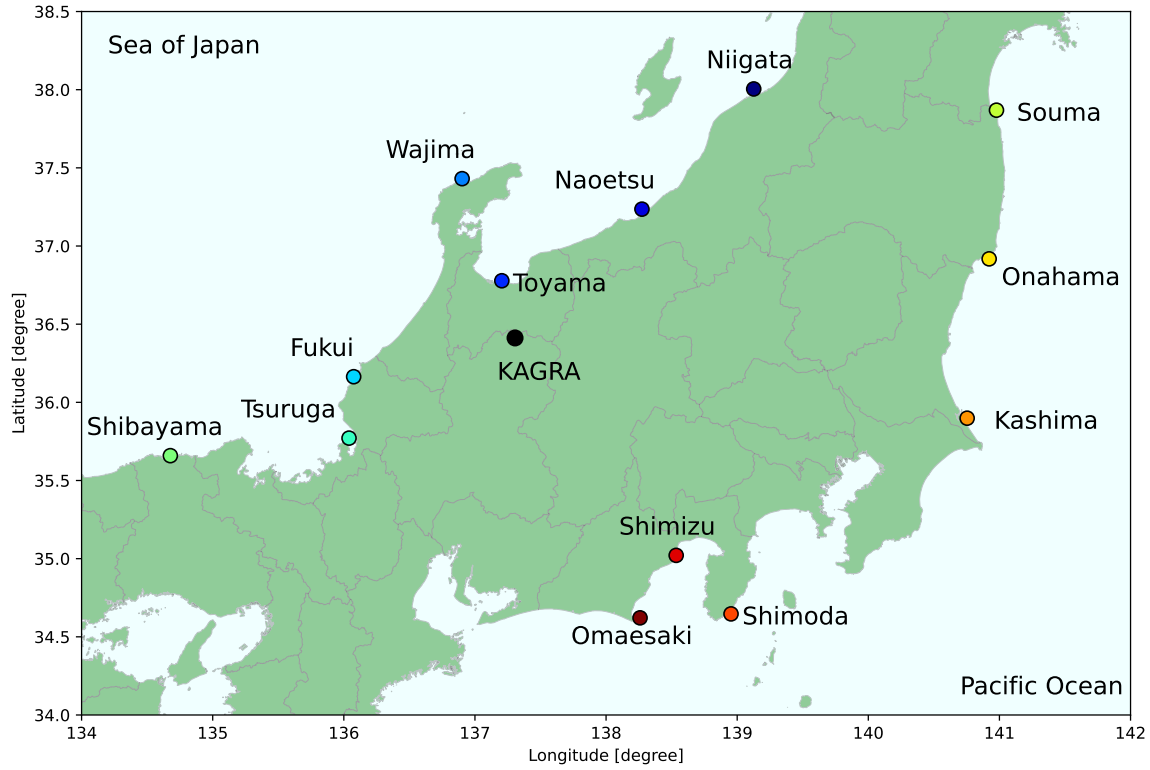


**Fig. 3** The time ratio for every week in 2020, classified by the microseismic motion level into three ranges: below  $0.3 \mu\text{m/s}$  (green),  $0.3\text{--}0.5 \mu\text{m/s}$  (yellow), and above  $0.5 \mu\text{m/s}$  (red). This classification is based on the lock-state of KAGRA in the O3GK [12].

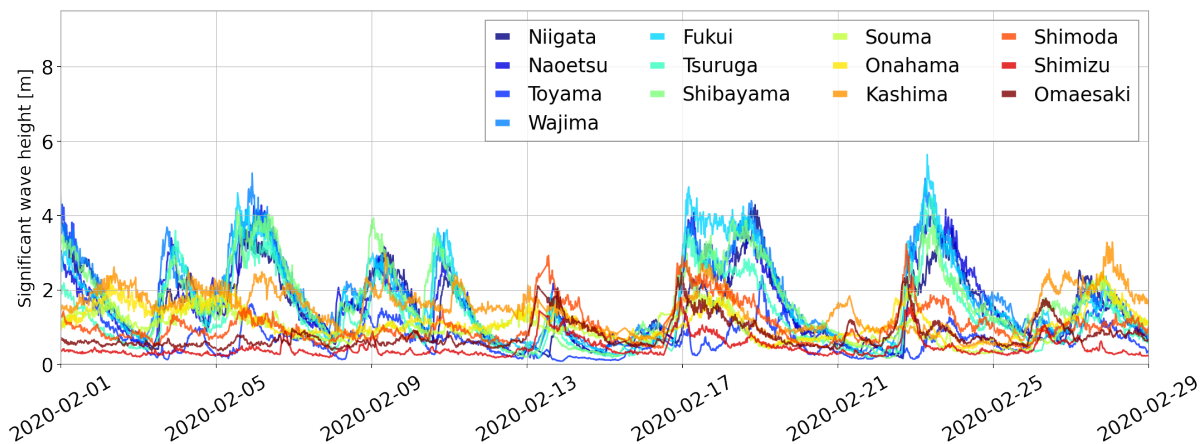
is Soma, about 350 km away from the KAGRA site. Fig. 5 shows the time series of the SWH at these 13 sites in February 2020 and Fig. A1 (in Appendix A.) shows them throughout 2020.

Fig. 6 shows the cumulative distribution functions of the SWH, which are normalized to ratios and subtracted from 1 to describe the behaviors at larger values of the SWH, at the four sites (Toyama, Wajima, Kashima, and Omaesaki) calculated every three months.<sup>1</sup> The waves are relatively larger in the winter seasons at Wajima and Toyama, which is consistent with the fact that the wind in the Sea of Japan is strongly affected by seasonal wind and becomes stronger in these seasons. Seasonal winds blow from the northwest during winter and from the southeast during summer in Japan. Toyama Bay is traditionally known as a “quiet bay”, and its SWH values are smaller than those of Wajima, even though these sites are close. In Kashima, wave activities seem to be at the same level, except during the summer period. At Omaesaki, there was little change throughout the year approximately 90% of the probability. Typhoons typically approach Japan between July and October. For

<sup>1</sup> Only four sites are shown in Fig. 6 because the SWH at each site has a strong positive correlation with the other sites and shows similar trends. See Fig. 8 for details.



**Fig. 4** Locations of the KAGRA (black marker) and the NOWPHAS observatories used in this study (color markers): Niigata, Naoetsu, Toyama, Wajima, Fukui, Tsuruga, and Shibayama on the Sea of Japan side, and Soma, Onahama, Kashima, Shimoda, Shimizu, and Omaesaki on the Pacific side.



**Fig. 5** Time series of the significant wave heights (SWH) during February 2020, provided by NOWPHAS [24]. All data for 2020 are shown in the A.

example, Fig. 7 shows the SWH when a typhoon approached Japan in 2019. The SWH on the Pacific Ocean side can reach approximately 10 m.

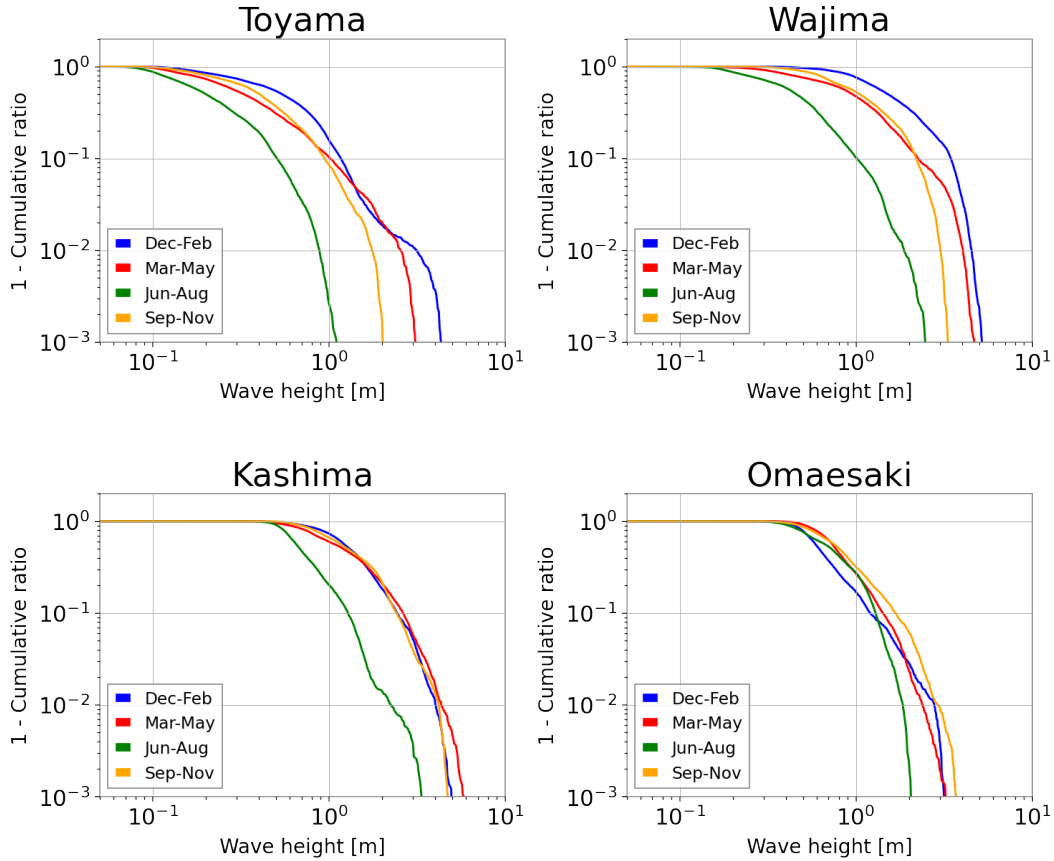


**Fig. 6** The cumulative distribution functions of the SWH, which are normalized to ratios and subtracted from 1 to describe the behaviors at larger values of the SWH, at the four sites (Toyama, Wajima, Kashima, and Omaesaki) for 2020, for each season: winter (January, February, and December), spring (from March to May), summer (from June to August), and autumn (from September to November).

Fig. 8 shows the correlation coefficients of SWH at the 13 sites. It suggests that the ocean waves around KAGRA can be categorized into three areas: the Sea of Japan side, the Pacific side of the coast facing east (Pacific side east), and the Pacific side of the coast facing south (Pacific side south). As these three groups have little correlation, it can be understood that their behaviors are independent.

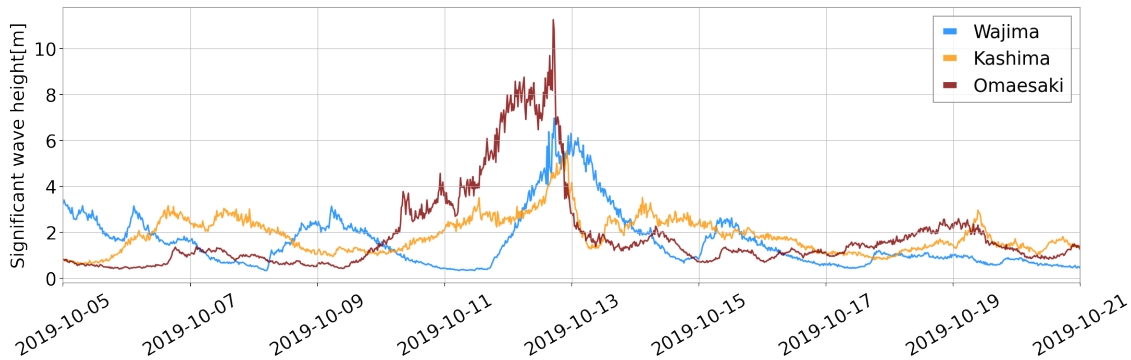


**Fig. 7** Time series of the significant wave heights (SWH) at three sites (Wajima, Kashima, and Omaesaki), during the typhoon period in October 2019.

#### 4 Estimation of the microseismic motion from the ocean wave

Data analysis utilizes seismometer data from KAGRA and ocean wave data. Both datasets were collected in 2020. Data during earthquake occurrence or approaching typhoons were excluded to ensure accuracy in the analysis. To evaluate the relationship between microseismic motion at KAGRA and ocean waves, correlation analysis between seismometer signals and SWH at each coast was conducted. Fig. 9 shows correlation coefficients between the microseismic motion at the KAGRA site and the SWH data from NOWPHAS described in Sections 2 and 3. It indicates a strong positive correlation with the Sea of Japan and a weak positive correlation with the Pacific Ocean. This is expected as KAGRA is approximately 70 km from the Sea of Japan and 200 km from the Pacific Ocean at their closest points. We aim to establish a simple equation relating ground velocity BLRMS  $v(t)$  and SWH  $H_{1/3}(t)$ . For instance, Ferretti *et al.* introduced the following equation:

$$H_{1/3}(t) = \exp \left[ a + b \ln v(t) \right], \quad (1)$$

where constants  $a = 9.48$  and  $b = 0.66$  were derived through fitting [26]. The objective of this section is to derive a similar equation between the microseismic motion at the KAGRA site and the SWH data in 2020 from NOWPHAS. Data during the typhoon period (Oct. 1 – Oct. 15) were excluded, except for the final validation in Fig. 13.

Here, we estimate the microseismic motion at the KAGRA site using wave data from 12 locations excluding Toyama Bay in NOWPHAS. In this study, the ground velocity BLRMS  $v$  and SWH  $H_{1/3}$  are squared to calculate energy. SWH data from nearby locations have a strong positive correlation, as shown in Fig. 8. To address data degeneracy, principal component analysis (PCA) is applied to three areas of the ocean: the Sea of Japan side

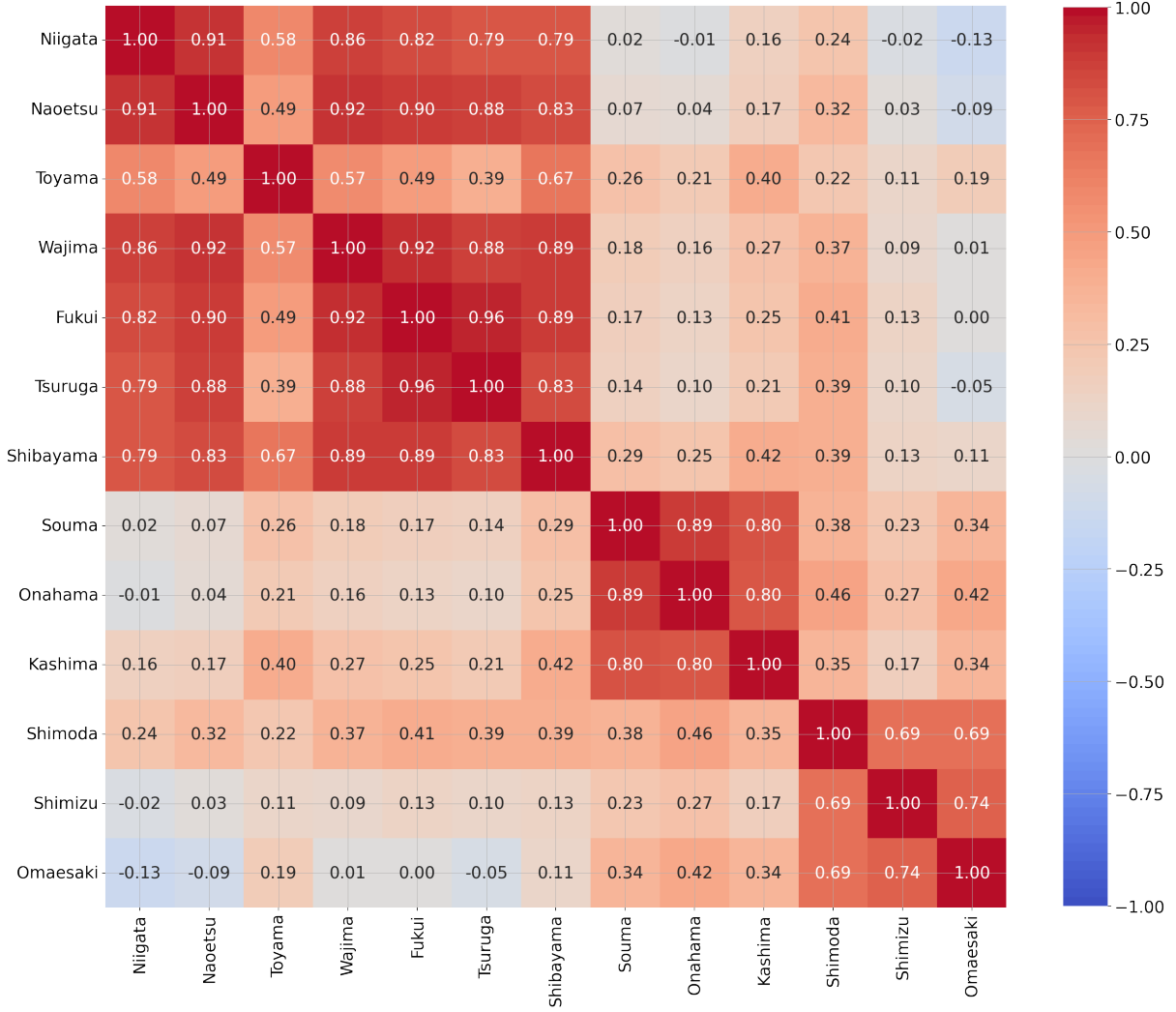


**Fig. 8** The Pearson correlation coefficient of the significant wave height (SWH) between the 13 coasts of Japan. The SWH data is collected every 20 minutes in 2020 and provided by the NOWPHAS [24].

(Niigata, Naoetsu, Wajima, Fukui, Tsuruga, and Shibayama), the eastern Pacific side (Soma, Onahama, and Kashima), and the southern Pacific side (Shimoda, Shimizu, and Omaesaki). Each squared SWH  $H_{1/3,j}^2(t)$  is standardized to have a mean of 0 and a standard deviation of 1.

$$x_j(t) = \frac{H_{1/3,j}^2(t) - \mu_j}{\sigma_j}, \quad (2)$$

where  $x_j(t)$  is the standardized wave data, and  $\mu_j$  and  $\sigma_j$  are the mean and the standard deviation of  $H_{1/3,j}^2(t)$  for the  $j$ -th NOWPHAS site. PCA (using `scikit-learn 1.0.2`) is performed for three areas (Sea of Japan side, eastern Pacific side, and southern Pacific side)

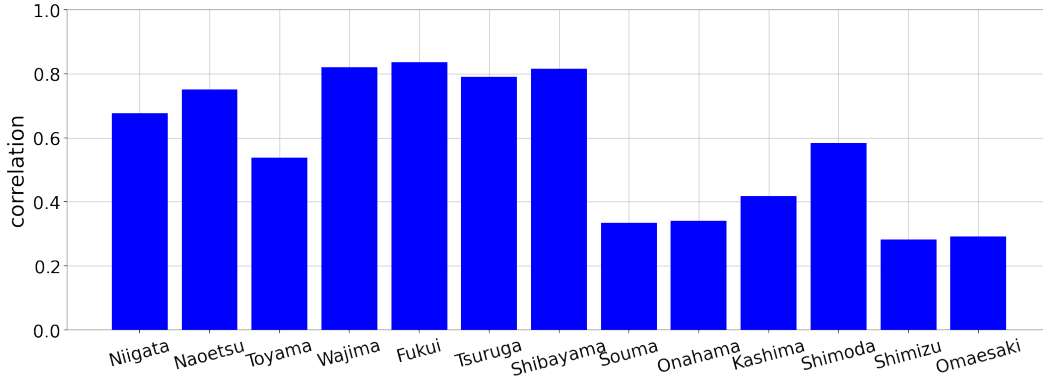


**Fig. 9** The Pearson correlation coefficient between the microseismic motion (BLRMS of the ground vibration velocity in 0.1–0.5 Hz) at the KAGRA site and the significant wave heights (SWH) in the NOWPHAS [24], for the 13 coasts in Japan. The data is every 20 minutes in 2020.

labeled by index  $i$ :

$$PC_i(t) = \sum_j c_{ij} x_j(t), \quad (3)$$

where  $PC_i(t)$  is the first-principal component, and  $c_{ij}$  is its eigenvector for the  $i$ -th area. The PCA parameter values are summarized in Table 1. These principal components  $PC_i(t)$  are difficult to compare to the microseismic motion because they are dimensionless and include negative values. Therefore, the weighted average of the squared SWH

$$\bar{H}_i^2(t) = \sum_j w_{ij} H_{1/3,j}^2(t), \quad w_{ij} = \frac{c_{ij}/\sigma_j}{\sum_k c_{ik}/\sigma_k}, \quad (4)$$

provides a better representation of the wave levels for each ocean area. Fig. 10 and Fig. 11 are the correlation plots and the correlation coefficients for the observed microseismic motion  $v_{\text{obs}}^2(t)$  and the wave levels of the three ocean areas  $\bar{H}_i^2(t)$ . There was no strong correlation between the individual representative significant wave heights. They also showed that waves on the Sea of Japan side strongly influence the ground vibration values.

The estimation for the microseismic motion at the KAGRA site is written as follows:

$$v_{\text{est}}^2(t) = \sum_i \alpha_i^2 \bar{H}_i^{2\beta_i}(t), \quad (5)$$

where  $\alpha_i$  and  $\beta_i$  are constants and are derived by fitting the data using the non-linear least squares method (via `scipy.optimize.curve_fit`). The results are shown in Fig. 12, where the red lines represent the estimated microseismic motion  $v_{\text{est}}^2(t)$  from the NOWPHAS data, and the black markers indicate the observed microseismic motion  $v^2(t)$  for one year in 2020.

**Table 1** Summary of the ocean wave data.  $\mu$  and  $\sigma$  represent the mean and standard deviation of the squared wave heights, respectively.  $c_{ij}$  represents the PCA eigenvectors for three areas: the Sea of Japan side, the Eastern Pacific side, and the Southern Pacific side.

	$\mu$ [m <sup>2</sup> ]	$\sigma$ [m <sup>2</sup> ]	$c_{ij}$		
			Sea of Japan	Eastern Pacific	Southern Pacific
Niigata	1.7	3.1	0.39	–	–
Naoetsu	1.8	3.1	0.42	–	–
Wajima	2.3	3.5	0.43	–	–
Fukui	2.3	3.9	0.42	–	–
Tsuruga	1.3	2.5	0.40	–	–
Shibayama	2.2	3.3	0.39	–	–
Soma	1.2	1.8	–	0.58	–
Onahama	1.5	2.1	–	0.58	–
Kashima	2.4	3.3	–	0.57	–
Shimoda	1.0	1.0	–	–	0.58
Shimizu	0.26	0.32	–	–	0.59
Omaesaki	0.91	1.09	–	–	0.57

The values of the fitting parameters are shown in Table 2. There is almost good agreement between the estimation and the observed data, except for the typhoon data not used in the PCA and the fitting. The values of the index  $\beta_i$  are close to  $b^{-1} \sim 1.5$  of Ferretti *et al.* [26].

**Table 2** The results of the fitting parameters in Eq. (5).

	$\alpha_i$ [ $\mu\text{m/s/m}^{\beta_i}$ ]	$\beta_i$
Sea of Japan	$0.358 \pm 0.001$	$1.314 \pm 0.005$
Eastern Pacific	$0.104 \pm 0.002$	$1.644 \pm 0.024$
Southern Pacific	$0.092 \pm 0.002$	$1.687 \pm 0.024$

To discuss the accuracy of this estimation, Fig. 13 (left) shows a histogram of the difference between the estimated and observed microseismic motion. It is almost a Gaussian distribution with a mean and standard deviation of  $1.2 \times 10^{-3} \mu\text{m/s}$  and  $7.4 \times 10^{-2} \mu\text{m/s}$ , respectively. This standard deviation was used for the error band in Fig. 12. Fig. 13 (right) shows a 2D histogram of the data points between the estimated and observed microseismic motions, confirming good linearity for most parts. This accuracy is achieved owing

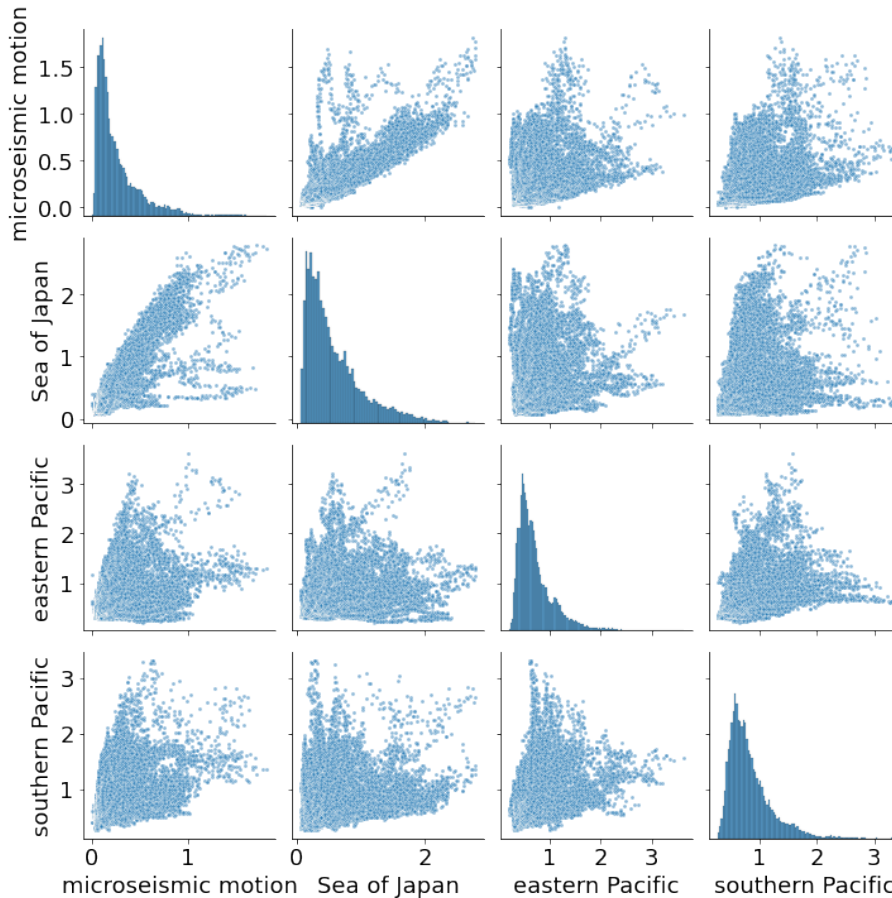


**Fig. 10** Scatter plot matrix of the observed microseismic motion at the KAGRA site and the representative wave levels for the Sea of Japan, the eastern Pacific side, and the southern Pacific side.

to the index parameter  $\beta_i$ ; if not used (corresponding to  $\beta_i = 1$ ), the estimation becomes systematically smaller when the ocean waves are violent. The cluster distributes around  $v_{\text{est}} \sim 0.3 \mu\text{m/s}$  and  $v_{\text{obs}} > 0.7 \mu\text{m/s}$  corresponding to the period when the typhoon was approaching Japan (during October 9–11). This is because an offshore typhoon directly shakes the seabed just below it, and microseismic waves propagate to Japan even though the coasts are still not rough [27].

## 5 Conclusion and prospects

In this study, we investigated the properties of the microseismic motion at the KAGRA site and the significant wave heights on the coasts of Japan measured and released by NOW-PHAS for 2020. The degeneracy of the wave data was resolved using a principal component

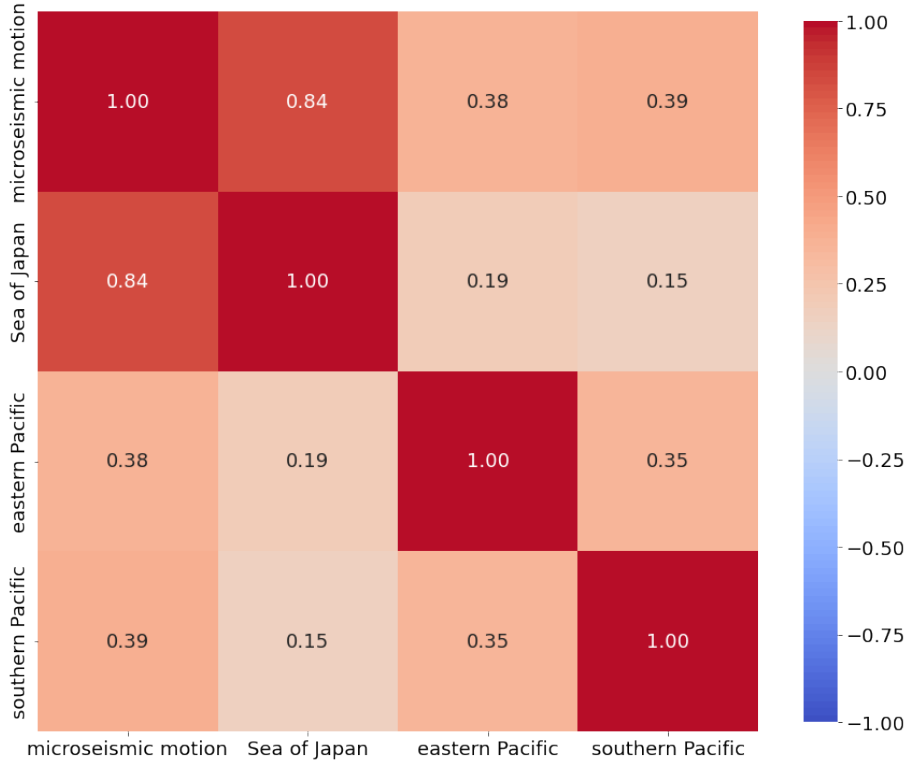


**Fig. 11** Correlation coefficient among the observed microseismic motion at the KAGRA site and the representative wave levels for the Sea of Japan, the eastern Pacific side, and the southern Pacific side.

analysis, and the first principal components of the three ocean regions were extracted. Microseismic motion observed at the KAGRA site was estimated by the combination of these components of the ocean waves within the standard deviation of  $7 \times 10^{-2} \mu\text{m/s}$ .

In this paper, only the first principal components for each sea area are used, and other principal components (which contain the local information) are not considered. Models that incorporate all information may provide better estimation accuracy. Other kinds of data, such as significant wave periods and wind direction, are also important. Machine learning is a possible way to improve this analysis. To include typhoon days, the development of special treatments is necessary, *e.g.*, using the position and magnitude of the typhoon.

A useful application of this study is *the microseismic forecast*. Future microseismic motion can be forecasted by inputting wave information from commercial weather forecasts into our equation. Fig. 14 shows an example of a microseismic forecast using a 1-week weather forecast on the website [0tenki.com](http://0tenki.com) provided by Bellsystem24 Inc [28]. The blue line represents the forecast with the error band of microseismic motion at the KAGRA site. The vertical

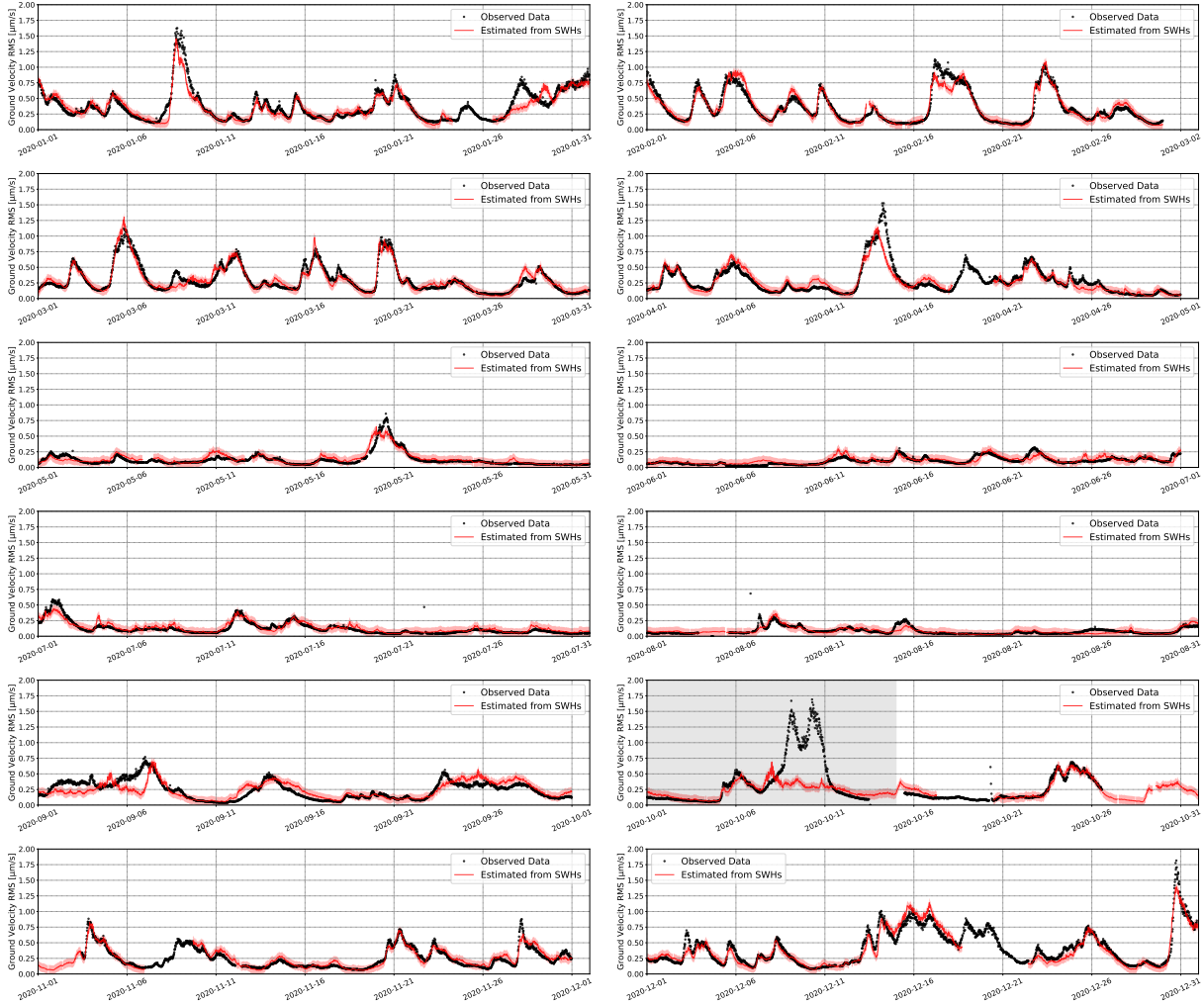


**Fig. 12** Comparison of the microseismic motion at the KAGRA site, between the observed data (black) and the estimation from the ocean waves (red, with the  $1\sigma$  error band). The typhoon period (Oct. 1 – Oct. 15, gray hatched) is not used for the estimation.

black dotted line represents the current time, and the right and left-hand sides represent the future and past, respectively. The horizontal dotted lines (red and yellow) correspond to the benchmark microseismic levels discussed in Section 2. The record of the historical forecast value is overlaid with BLRMS of the actual measured values, allowing users to assess the accuracy of the recent forecast. This plot is automatically updated and shown on a website (internal page) and contributes to commissioning works at the KAGRA observatory, especially for its scheduling.

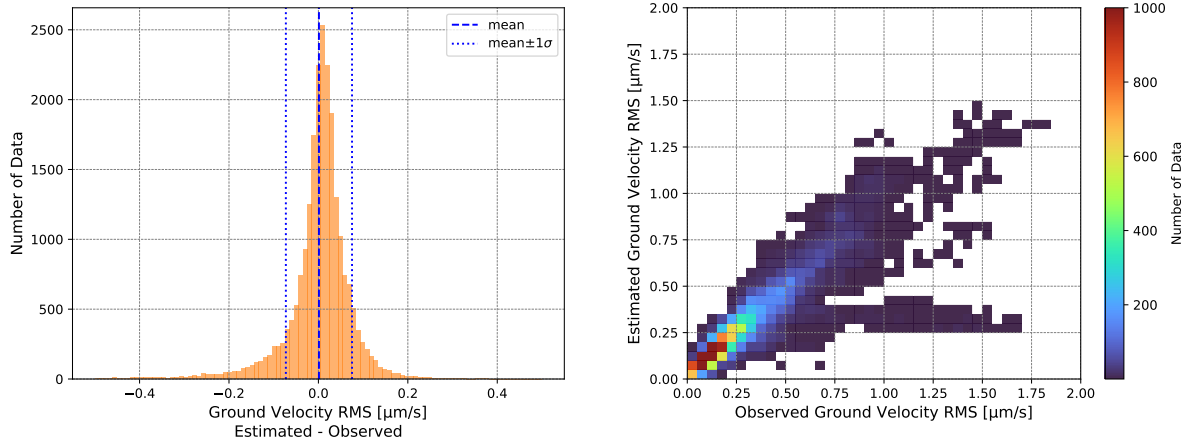


**Fig. 13** Left: Histogram of the difference between observed values and estimated values of the microseismic motion. Right: 2D histogram of the observed values and estimated values of the microseismic motion.

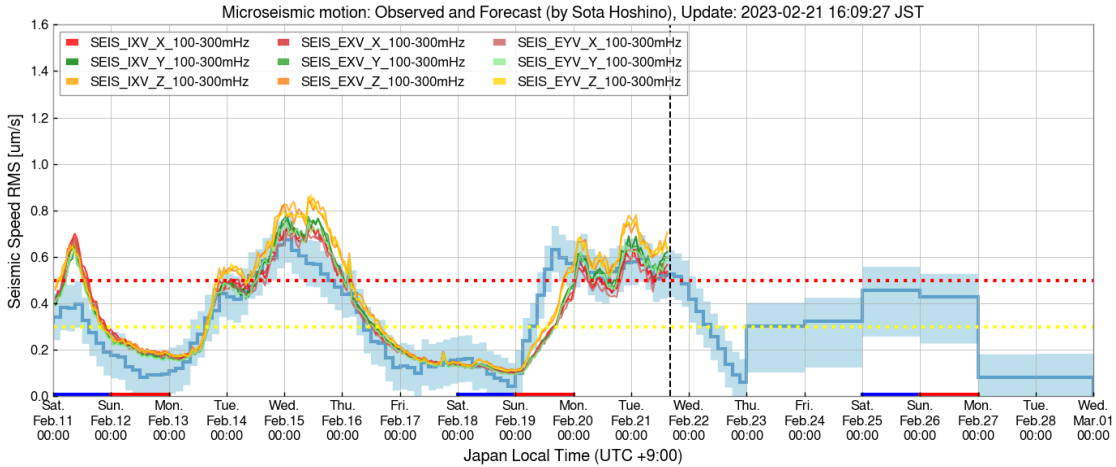


**Fig. 14** An example of the microseismic forecast graph. The black line shows the current date, in this case, 2023-05-18 11:09 (JST). The right and left sides of it are the future and past, respectively. The horizontal dotted lines (red and yellow) correspond to the benchmark microseismic level discussed in Sec. 2, red is  $0.5 \mu\text{m/s}$ , and yellow is  $0.3 \mu\text{m/s}$ . The historical data is overlaid with BLRMS of the actual measured triaxial ground vibrations from the three seismometers located at the KAGRA site for comparison.

## Acknowledgement

This research has made use of data, software, and web tools obtained or developed by the KAGRA Collaboration, especially the administrators of the digital system, and managers

of the KAGRA site. The NOWPHAS data is provided by the Port and Harbor Bureau, Ministry of Land, Infrastructure, Transport and Tourism, Japan, and the weather forecast data is provided by Bellsystem24 Inc.

The KAGRA project is supported by MEXT, JSPS Leading-edge Research Infrastructure Program, JSPS Grant-in-Aid for Specially Promoted Research 26000005, JSPS Grant-in-Aid for Scientific Research on Innovative Areas 2905: JP17H06358, JP17H06361 and JP17H06364, JSPS Core-to-Core Program A. Advanced Research Networks, JSPS Grant-in-Aid for Scientific Research (S) 17H06133 and 20H05639, JSPS Grant-in-Aid for Transformative Research Areas (A) 20A203: JP20H05854, the joint research program of the Institute for Cosmic Ray Research, University of Tokyo, National Research Foundation (NRF), Computing Infrastructure Project of Global Science experimental Data hub Center (GSDC) at KISTI, Korea Astronomy and Space Science Institute (KASI), and Ministry of Science and ICT (MSIT) in Korea, Academia Sinica (AS), AS Grid Center (ASGC) and the National Science and Technology Council (NSTC) in Taiwan under grants including the Rising Star Program and Science Vanguard Research Program, Advanced Technology Center (ATC) of NAOJ, and Mechanical Engineering Center of KEK. Especially this work was founded by JSPS Grant-in-Aid for JSPS Fellows 19J01299 and the Joint Research Program of the Institute for Cosmic Ray Research (ICRR) University of Tokyo 2020-G07, 2020-G12, 2020-G21, 2021-G07, 2021-G09, 2021-G10, 2022-G07, 2022-G12, 2022-G21.

We would like to thank Editage ([www.editage.com](http://www.editage.com)) for English language editing.

## References

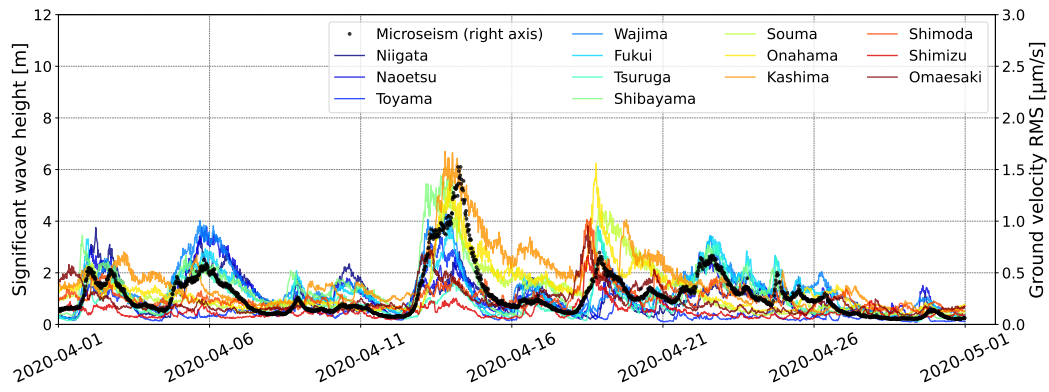
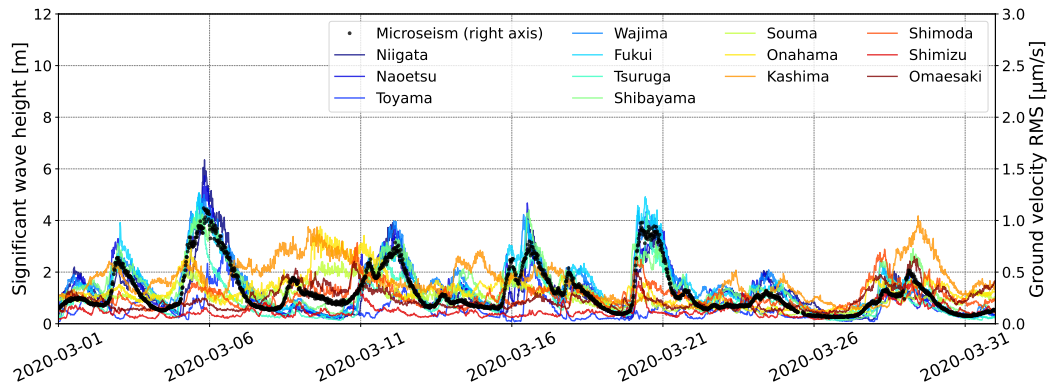
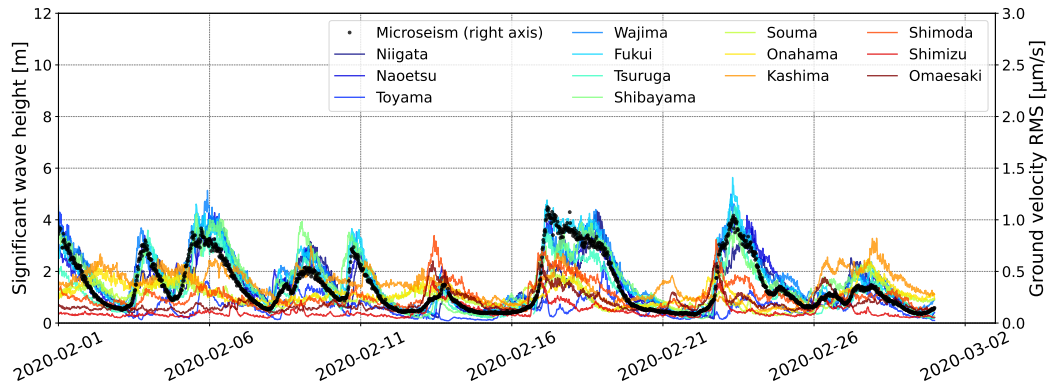
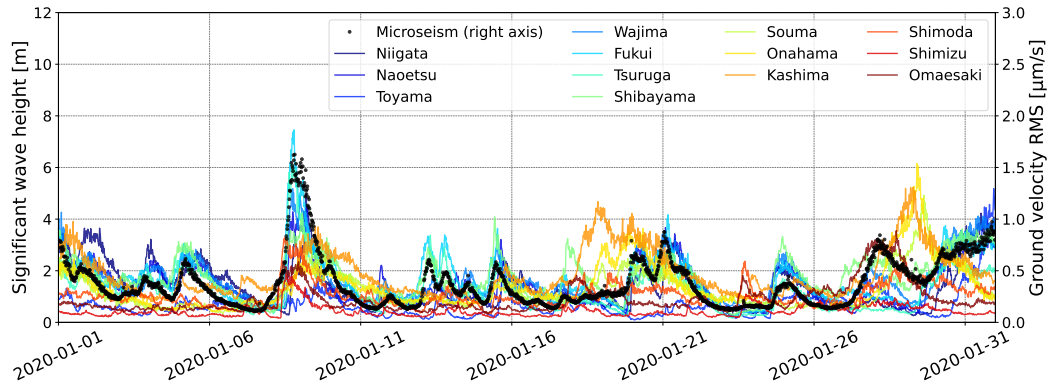
- [1] The LIGO Scientific Collaboration, *Class. Quantum Grav.* **32** 074001 (2015).
- [2] B. P. Abbott et al. (LIGO Scientific Collaboration and Virgo Collaboration), *Phys. Rev. Lett.* **116**, 131103 (2016).
- [3] F. Acernese et al., *Class. Quantum Grav.* **32** 024001 (2015).
- [4] B. P. Abbott et al. (LIGO Scientific Collaboration and Virgo Collaboration), *Phys. Rev. Lett.* **119**, 141101 (2017).
- [5] B. P. Abbott et al. (LIGO Scientific Collaboration and Virgo Collaboration), *Phys. Rev. Lett.* **119**, 161101 (2017).
- [6] T. Akutsu et al. (KAGRA Collaboration), *Prog. Theor. Exp. Phys.* **2021**, 5, 05A1015 (2021).
- [7] T. Akutsu et al. (KAGRA Collaboration), *Prog. Theor. Exp. Phys.* **2020**, 5, 053F01 (2020).
- [8] T. Akutsu et al., *Class. Quantum Grav.* **36**, 165008 (2019).
- [9] T. Akutsu et al., *Prog. Theor. Exp. Phys.* **2018**, 1, 013F01 (2018).
- [10] K. Kokeyama on behalf of the KAGRA collaboration, *Proceedings of the 3rd World Summit on Exploring the Dark Side of the Universe (EDSU2020)*, March 9–13, 2020, Guadeloupe Islands, p.41–48.
- [11] H. Abe et al. (KAGRA Collaboration), *Galaxies* **2022**, 10(3), 63 (2022).
- [12] Y. Fujikawa, Master thesis, Niigata University (2021) [JGW-L2012423-v12, in Japanese].
- [13] M. S. Longuet-Higgins, *Philosophical Transactions of the Royal Society of London* **243**, 857 (1950), p.1–35.
- [14] K. Hasselmann, *Rev. Geophys* **1**, 2 (1963), p.177–210.
- [15] T. Tanimoto, *Geophys. J. Int.* **168**, 2 (2007), p.571–582.
- [16] T. Tanimoto, *Geophys. Res. Lett.* **34**, 5, L05308 (2007).
- [17] P. D. Bromirski et al., *J. Geophys. Res.* **104**(C9), 20753–20766 (1999).
- [18] F. Badaracco et al., *Phys. Rev. D* **104**, 042006 (2021).
- [19] S. Miyoki, on behalf of the KAGRA collaboration, *Proc. SPIE* 11445, *Ground-based and Airborne Telescopes*

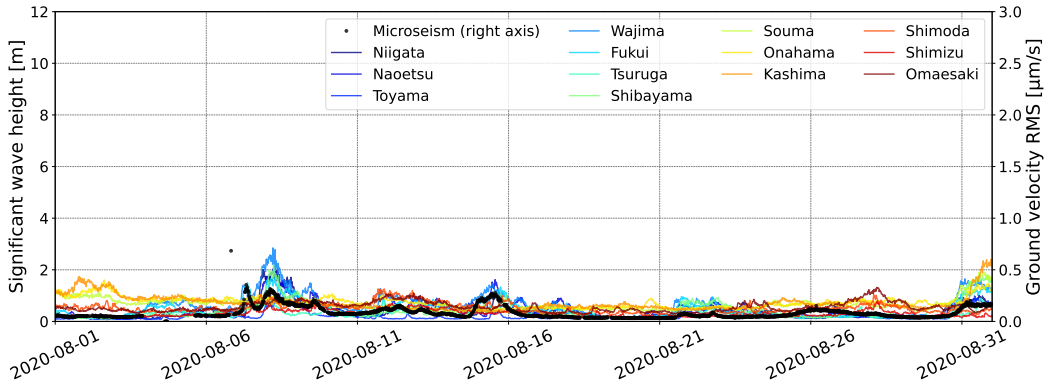
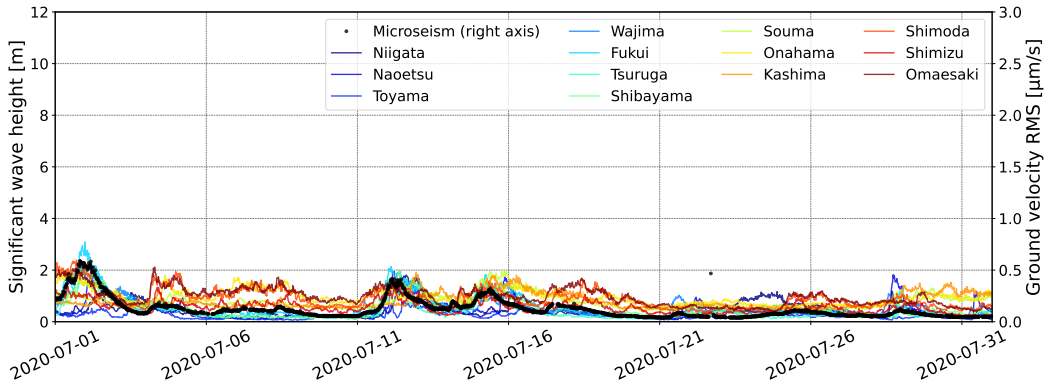
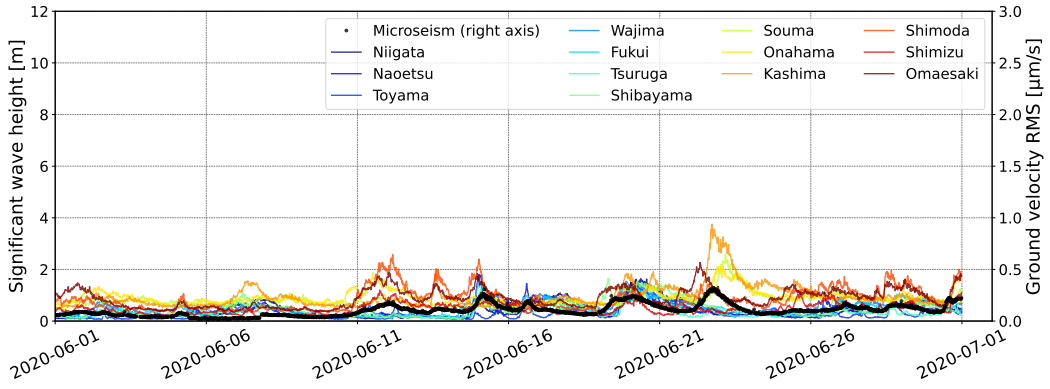
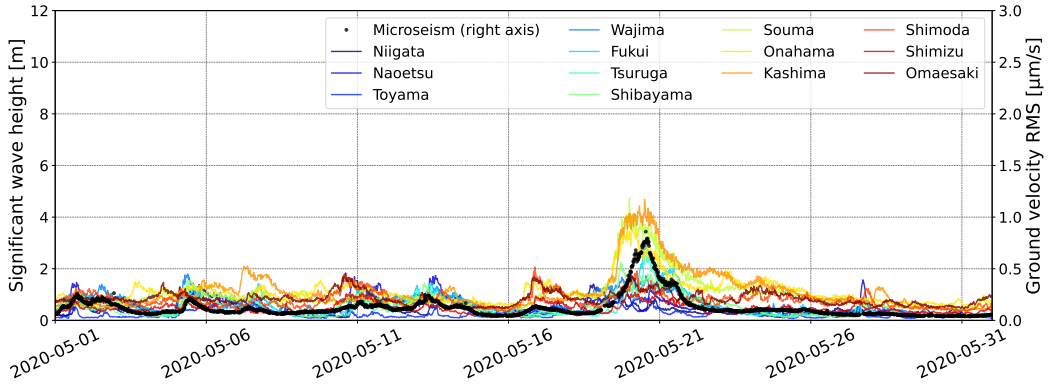
VIII, 114450Z (13 December 2020), p.192–204.

- [20] J. R. Peterson, U.S. Geol. Surv. Open-File Rept. 93–322 (1993).
- [21] T. Washimi et al., Prog. Theor. Exp. Phys. **2022**, 11, 113H02 (2022).
- [22] A. Longo et al., Pure Appl. Geophys. **178**, 3461–3470 (2021).
- [23] Significant Wave Height, National Weather Service [https://www.weather.gov/key/marine\\_sigwave](https://www.weather.gov/key/marine_sigwave)
- [24] The Nationwide Ocean Wave information network for Ports and HARbourS, NOWPHAS, [https://www.mlit.go.jp/kowan/nowphas/index\\_eng.html](https://www.mlit.go.jp/kowan/nowphas/index_eng.html)
- [25] Y. Hida et al., Fisheries Engineering **54**, 3, 173–184 (2017).
- [26] G. Ferretti et al., Geophys. J. Int. **194**, 1, 524–533 (2013).
- [27] J. Zhang et al, Geophys. Res. Lett. **37**, 15, L15301 (2010).
- [28] Otenki.com, Bellsystem24, Inc., <https://hp.otenki.com/>

## A One year data of the SWH and the microseismic motion

Appendix A contains SWH time series data for the full year 2020 that were not shown in Fig. 5. In addition, this figure overlays the BLRMS of the KAGRA seismometer data.





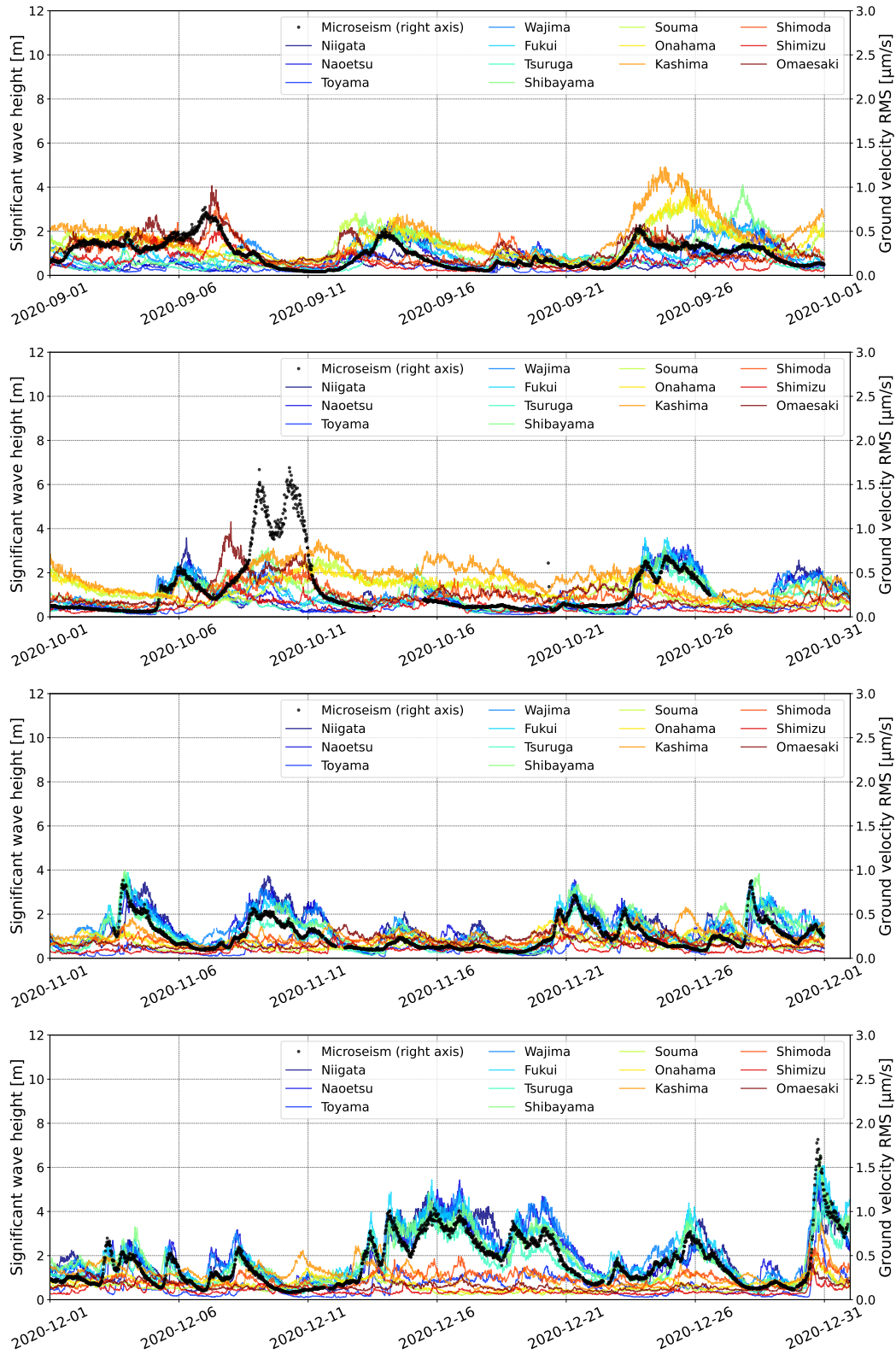


**Fig. A1** The time series data of the SWH in NOWPHAS and the microseismic motion at the KAGRA site, partially shown in Fig. 5, are shown here through the full year 2020.

# Evaluation of the microseismic motion at the KAGRA site based on the ocean wave data

S.Hoshino<sup>\*,1</sup>, Y.Fujikawa<sup>1</sup>, M.Ohkawa<sup>1</sup>, T.Washimi<sup>+,2</sup>,  
T.Yokozawa<sup>3</sup>

<sup>1</sup>Faculty of Engineering, Niigata University, 8050 Ikarashi-2-no-cho, Nishi-ku, Niigata City, Niigata 950-2181, Japan

<sup>2</sup>Gravitational Wave Science Project (GWSP), Kamioka branch, National Astronomical Observatory of Japan (NAOJ), Kamioka-cho, Hida City, Gifu 506-1205, Japan

<sup>3</sup>Institute for Cosmic Ray Research (ICRR), KAGRA Observatory, The University of Tokyo, Kamioka-cho, Hida City, Gifu 506-1205, Japan

\*First author

E-mail: \*f22c036a@mail.cc.niigata-u.ac.jp, +tatsuki.washimi@nao.ac.jp

**Abstract.** The microseismic motion, which is the ambient ground vibration caused by ocean waves, affects ground-based gravitational detectors. In this study, characteristics of the ocean waves such as seasonal variations and correlation coefficients were investigated for the significant wave heights at 13 coasts in Japan. The relationship between the ocean waves and the microseismic motion at the KAGRA site was also evaluated. As a result, it almost succeeded to explain the microseismic motion at the KAGRA site by the principal components of the ocean wave data. One possible application of this study is the microseismic forecast and its example is also shown.

## 1. Introduction

Gravitational waves are ripples of space-time distortion propagating at the speed of light and their direct observation is a key probe in advanced astronomy. The first successful detection was performed in 2015 by the advanced Laser Interferometer Gravitational-Wave Observatory (LIGO, USA) [1, 2], and the first simultaneous detections by LIGO and Virgo (Italy) was performed in 2017 [3, 4, 5]. Kamioka Gravitational Wave Detector (KAGRA) is a laser interferometric gravitational wave detector with 3 km arms in Japan [6]. Two solo observation runs in 2015 and 2018 [7, 8] and the first international joint observation run (O3GK) with the GEO 600 in Germany were performed during April 7–21, 2020 [9, 10, 11]. KAGRA has two unique features compared with other kilometer-scale detectors in the world: (1) it is constructed underground at the Kamioka to reduce the ground vibration noise, (2) the test mass mirrors are cooled down to reduce thermal noise. To attain and maintain the working point of the detector, all mirror positions, angles, and motions must be controlled. When external disturbances

37 occur, it becomes difficult for the interferometer to maintain these controls, and the  
38 resonant state is broken. Consequently, the gravitational wave observations must be  
39 stopped. This state is called "lock loss" and a reduction in the lock loss rate is important  
40 for performing meaningful observations. During the O3GK period in KAGRA, it was  
41 occasionally difficult to keep the interferometer locked state when microseismic motions,  
42 which are ground vibrations with a frequency range of about 0.1–0.5 Hz induced by the  
43 ocean waves, were large [11, 12, 13]. The mechanism of microseismic motion excited  
44 by ocean waves was derived by Longuet-Higgins [14] and approximated using a non-  
45 linear equation extended by Hasselmann [15]. This approximation was evaluated using  
46 the normal-mode equation derived by Tanimoto to obtain negligible errors for ground  
47 vibrations occurring in the ocean to a depth of approximately 1 km [16, 17]. Microseismic  
48 motion is related to the amplitude and period of the waves, with the period of the ground  
49 motions being approximately twice the period of the waves, and the magnitude of the  
50 motions being derived from the energy of the waves, as shown by Bromirski *et al.* [18].

51 In this study, we investigate the relationship between the microseismic motion  
52 at the KAGRA site and the activity of the ocean waves around Japan, it has been  
53 expected qualitatively but has not been studied quantitatively. Sec. 2 explains the details  
54 of the seismometers installed at the KAGRA site and the behavior of the measured  
55 microseismic motion. In Sec. 3, the characteristics of the ocean waves around Japan  
56 are discussed based on public data. In Sec. 4, we propose an approximate equation  
57 connecting the microseismic motion at the KAGRA site to the wave height at various  
58 coasts in Japan. Finally, in Sec. 5, the results of this study are summarized and its  
59 useful application, a forecast of future microseismic motion, is shown.

## 60 **2. Characterizations for the microseismic motion at the KAGRA site**

61 In this section, information about the seismometers used in this study and the  
62 characteristics of their data are explained. To monitor the environments around the  
63 KAGRA interferometer, several sensors were located at the experimental site and  
64 continuously logged using the KAGRA DAQ system [19]. Three seismometers were  
65 located at each end and corner station and the horizontal axes were aligned with  
66 the orientations of the arms [20]. The seismometers are the Trillium 120QA from  
67 *Nanometrics Inc.*, sensitive to the ground velocity in three directions from 0.01 Hz to  
68 10 Hz. Figure 1 shows examples of the amplitude spectral density (ASD) of the ground  
69 velocity of these seismometers in each location and direction. In this figure, two different  
70 days are shown to compare the high- and low-noise days, with black dashed lines, which  
71 are Peterson's high/low seismic noise model [21]. The significant peak at 0.1–0.5 Hz  
72 corresponding to the microseismic motion is clearly seen in all ASDs and its amplitude  
73 and structure are almost the same in the stations and the directions for both days. The  
74 amplitude below 0.05 Hz varies in the channels, and this behavior is assumed to be due  
75 to atmospheric pressure [22, 23]. Based on these results, for simplicity, the vertical  
76 signal of the seismometer located at the corner station was used as a representative of

77 the ground vibration in this study.

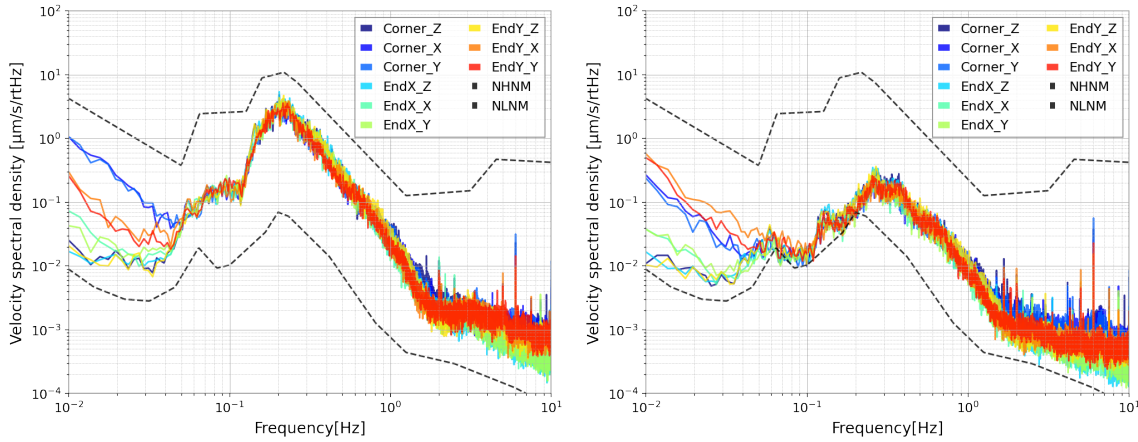


**Figure 1.** Amplitude spectral densities (ASDs) of the ground velocity, for each location (Corner, X-end, Y-end) and each direction (X, Y, Z) at the KAGRA site. The measurement time is 4096 seconds on February 18 (left) and June 10 (right) in 2020. Black dashed lines represent Peterson’s high/low seismic noise model [21].

78 The band-limited root mean square (BLRMS) of the seismometer signal was used to  
 79 evaluate the time dependence of the microseismic motion at the KAGRA site. BLRMS  
 80 is the root mean square every 20 minutes for the time series data filtered using a  
 81 bandpass filter (`TimeSeries.bandpass` in `gwpy 2.1.4`) from 0.1 Hz to 0.5 Hz, to limit  
 82 the frequency band. Figure 2 shows an example from February 2020. All the data for  
 83 2020 are shown in Appendix A. In the O3GK run, the KAGRA interferometer would be  
 84 difficult to be kept in a locked state when the BLRMS value is above  $0.3 \mu\text{m/s}$  and could  
 85 not be kept in the locked state at all when the BLRMS value became over  $0.5 \mu\text{m/s}$  [13].

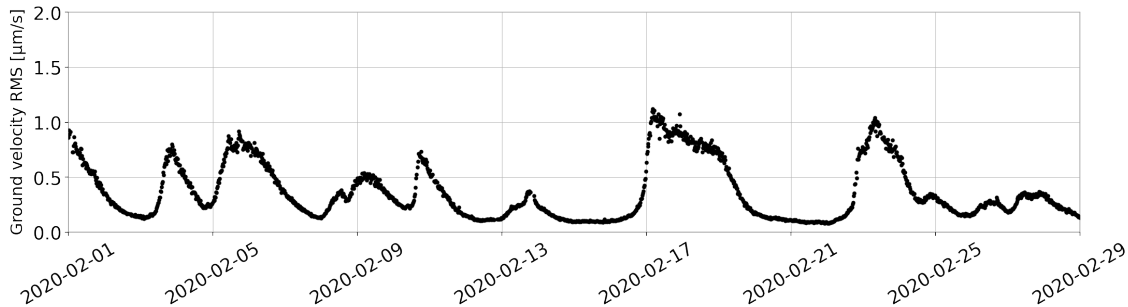


**Figure 2.** The root mean square of the microseismic motion (0.1–0.5 Hz) at the KAGRA site during February 2020. All data for 2020 are shown in the Appendix A.

86 Figure 3 shows the ratio of the microseismic motion for every week in 2020 into  
 87 the three ranges: below  $0.3 \mu\text{m/s}$  (green), between  $0.3 \mu\text{m/s}$  and  $0.5 \mu\text{m/s}$  (yellow),  
 88 and above  $0.5 \mu\text{m/s}$  (red). The microseismic motion increased from winter to the  
 89 beginning of spring (December–March) and remained stable at small values in summer.

90 It also shows large values at the beginning of autumn (September and October) owing  
 91 to typhoons.

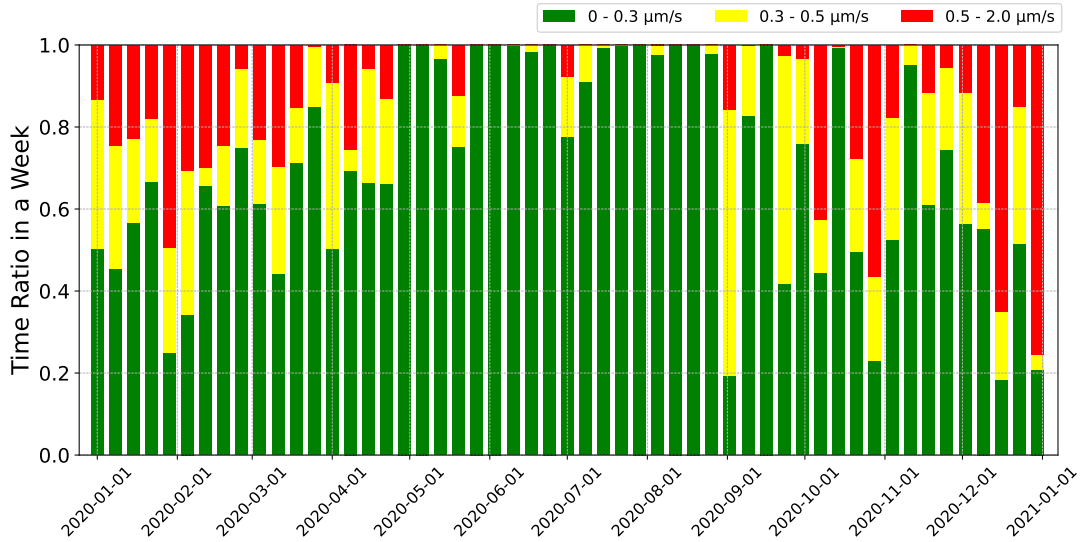


**Figure 3.** The ratio of the microseismic motion for every week in 2020 into the three ranges: below  $0.3 \mu\text{m/s}$  (green),  $0.3\text{--}0.5 \mu\text{m/s}$  (yellow), and above  $0.5 \mu\text{m/s}$  (red). This classification is based on the locked state of KAGRA in the O3GK [13].

### 92 3. Characterizations for the ocean waves around Japan

93 Significant wave heights (SHW,  $H_{1/3}$ ), which are the average of the highest 1/3 of the  
 94 waves over a period of time, are widely used as indicators of the strength of ocean  
 95 waves. Wave data are provided by the *Nationwide Ocean Wave information network for*  
 96 *Ports and Harbors* (NOWPHAS) operated by the *Port and Harbor Bureau, Ministry*  
 97 *of Land, Infrastructure, Transport and Tourism*, Japan [24]. NOWPHAS data were  
 98 measured every 20 minutes using the zero-up-cross method [25]. Seven sites on the Sea  
 99 of Japan coast (Niigata, Naoetsu, Toyama, Wajima, Fukui, Tsuruga, and Shibayama)  
 100 and six sites on the Pacific side (Soma, Onahama, Kashima, Shimoda, Shimizu, and  
 101 Omaesaki), as shown in Figure 4, are selected for use in this study from the NOWPHAS  
 102 data. Among the selected sites, the closest one is Toyama about 45 km, and the farthest  
 103 one is Soma about 350 km from the KAGRA site. Figure 5 shows the time series of the  
 104 SHW at these 13 sites throughout 2020.

105 Figure 6 shows the cumulative ratio (subtracted from 1) of the SWH at the four  
 106 sites (Toyama, Wajima, Kashima, and Omaesaki) calculated every three months. ‡  
 107 The waves are relatively larger in the winter seasons at Wajima and Toyama, which  
 108 is consistent with the fact that the wind in the Sea of Japan is strongly affected

‡ Only four sites are shown in Figure 6 because the SWH at each site have a strong positive correlation with the other sites and show similar trends. See Figure 8 for details.

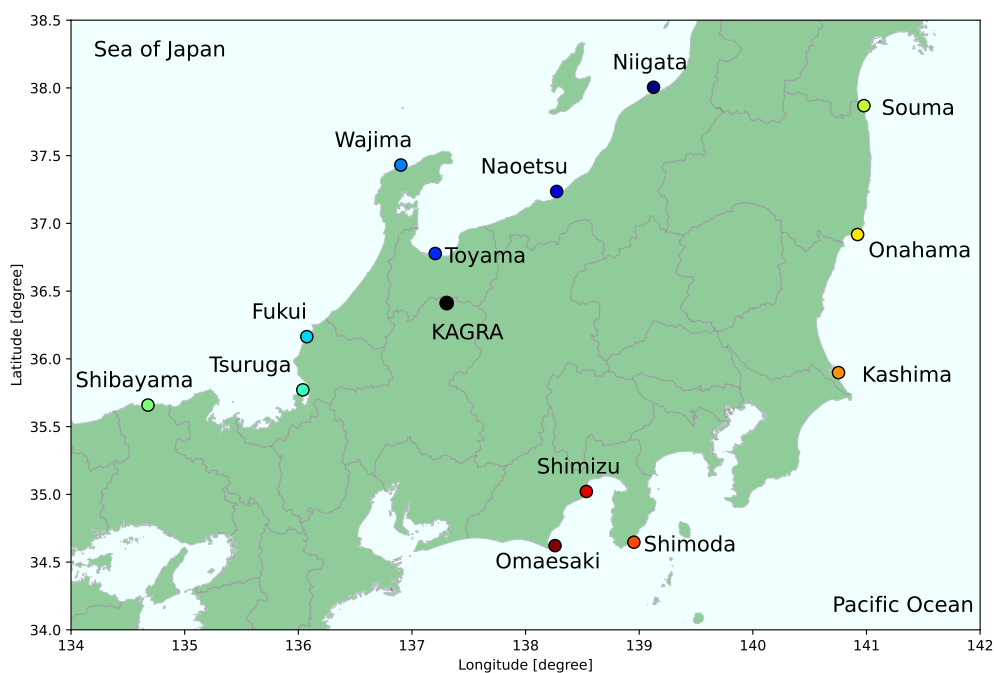


**Figure 4.** Locations of the KAGRA (black marker) and the NOWPHAS observatories used in this study (color markers): Niigata, Naoetsu, Toyama, Wajima, Fukui, Tsuruga, and Shibayama on the Sea of Japan side, and Soma, Onahama, Kashima, Shimoda, Shimizu, and Omaesaki on the Pacific side.

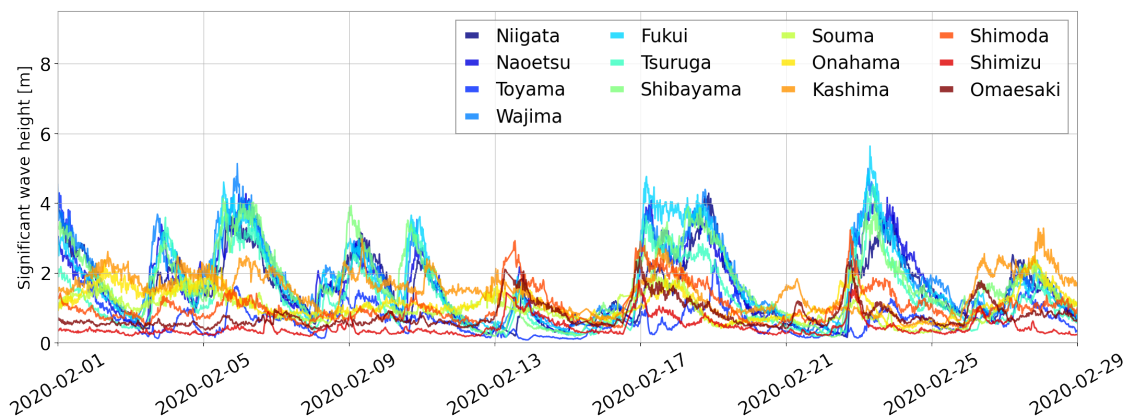


**Figure 5.** Time series of the significant wave heights (SHW) during February 2020, provided by NOWPHAS [24]. All data for 2020 are shown in the Appendix A.

109 by seasonal wind and becomes stronger in these seasons. Seasonal winds blow from  
 110 the northwest during winter and southeast during summer in Japan. Toyama Bay is  
 111 traditionally known as a "quiet bay" and its SWH values are smaller than those of  
 112 Wajima, even though these sites are close to each other. In Kashima, wave activities  
 113 seem to be at the same level, except for the summer period. At Omaesaki, there was  
 114 little change throughout one year approximately 90% of the probability. Typhoons  
 115 typically approached Japan between July and October. For example, Figure 7 shows  
 116 the SWH when a typhoon approached Japan in 2019. The SWH on the side of the

117 Pacific Ocean can reach approximately 10 m.

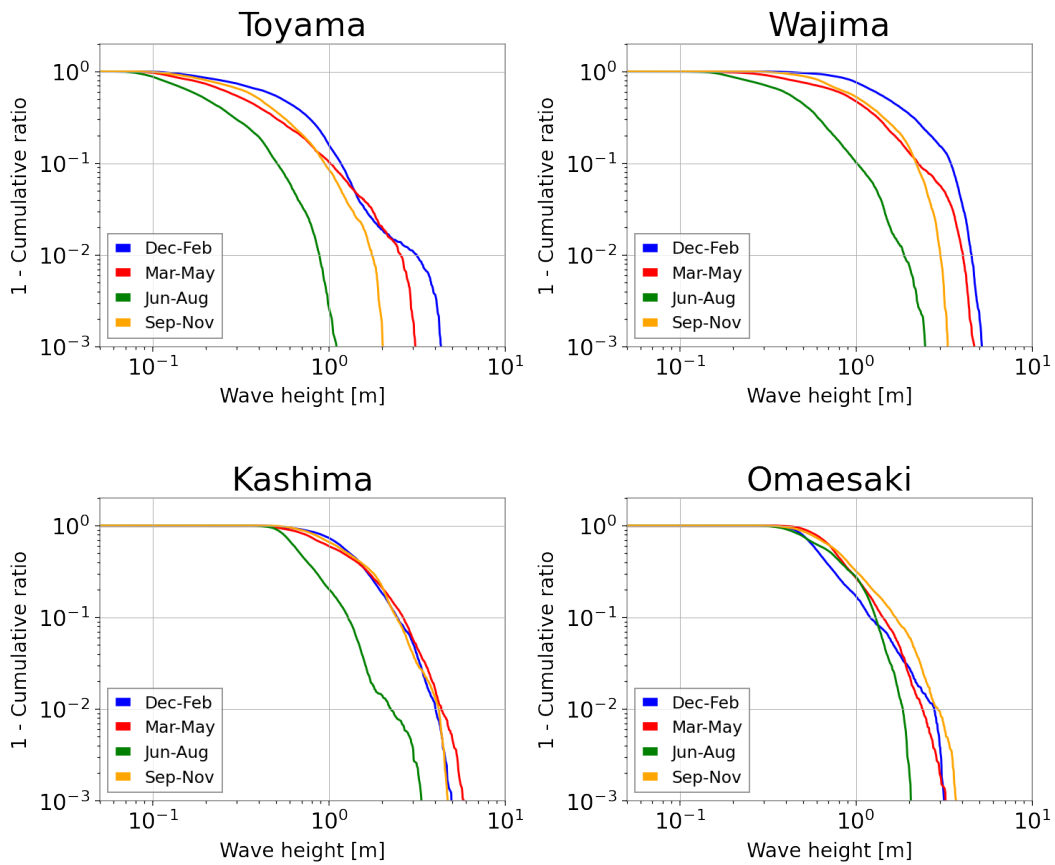


**Figure 6.** The cumulative ratio (subtracted from 1) of the SWH at the four sites (Toyama, Wajima, Kashima, and Omaesaki) for 2020, for each season: winter (January, February, and December), spring (from March to May), summer (from June to August), and autumn (from September to November).

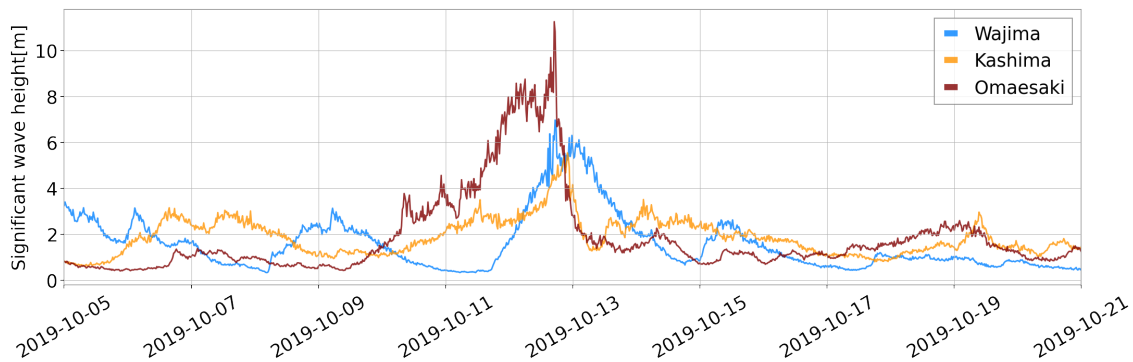


**Figure 7.** Time series of the significant wave heights (SHW) at three sites (Wajima, Kashima, and Omaesaki), during the typhoon period in October 2019.

118 Figure 8 shows the correlation coefficients of SWH at the 13 sites. It suggests that  
 119 the ocean waves around KAGRA can be categorized into three areas, the Sea of Japan

120 side, the Pacific side of the coast facing east (Pacific side east), and the Pacific side of  
 121 the coast facing south (Pacific side south). As these three groups have little correlation,  
 122 it can be understood that their behaviors are independent of each other.

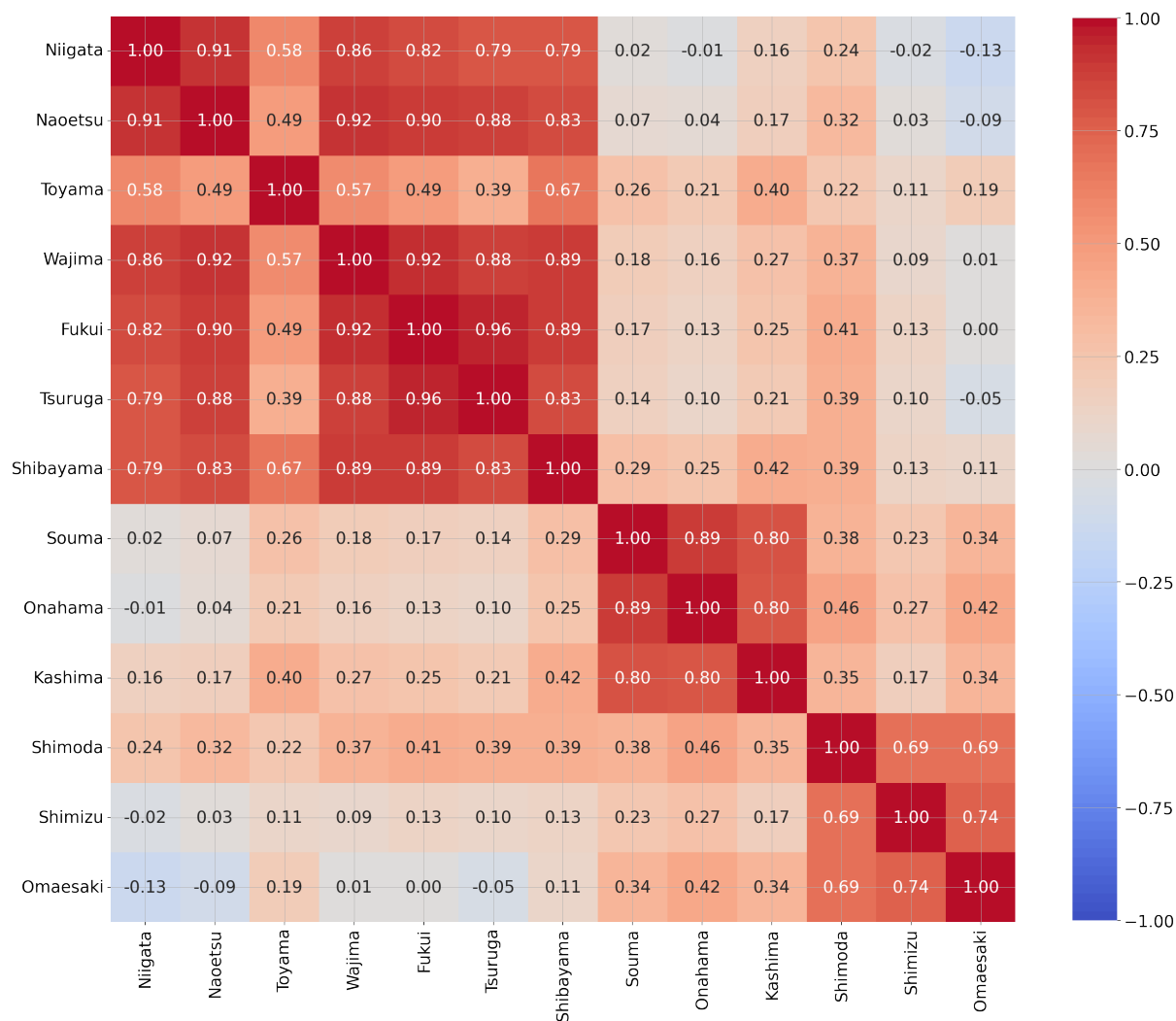


**Figure 8.** Correlation coefficient of the significant wave height (SWH) between the NOWPHAS sites used in this study.

#### 123 4. Prediction of the microseismic motion from the ocean wave

124 Data analysis is performed using seismometer data from KAGRA and ocean wave  
 125 data. Both the seismometer and ocean wave data were obtained in 2020. In addition,  
 126 data for the periods of earthquake occurrence or approaching typhoons are excluded  
 127 for a more accurate analysis. To evaluate (and investigate) the relationship between  
 128 microseismic motion at KAGRA and ocean waves, a correlation analysis between the  
 129 seismometer signal and SHW of each coast is performed. Figure 9 shows the correlation

130 coefficients between the microseismic motion at the KAGRA site and the SWH data  
 131 from NAOPHAS described in Sections 2 and 3. It shows a strong positive correlation  
 132 with the Sea of Japan and a weak positive correlation with the Pacific Ocean side. This  
 133 is reasonable because the KAGRA site is located about 70 km from the Sea of Japan at  
 134 the shortest distance, and about 200 km from the Pacific Ocean at the shortest distance.  
 135 It is expected that a simple equation between a BLRMS of ground velocity  $v$  and a SWH  
 136  $H_{1/3}$  is written. For instance, Ferretti et al. introduced the following equation:

$$137 \quad H_{1/3}(t) = \exp \left[ a + b \ln v(t) \right], \quad (1)$$

138 where constants  $a = 9.48$  and  $b = 0.66$  are derived by fitting [26]. The goal of this  
 139 section is to derive a similar equation between the microseismic motion at the KAGRA  
 140 site and the SWH data from NOWPHAS.

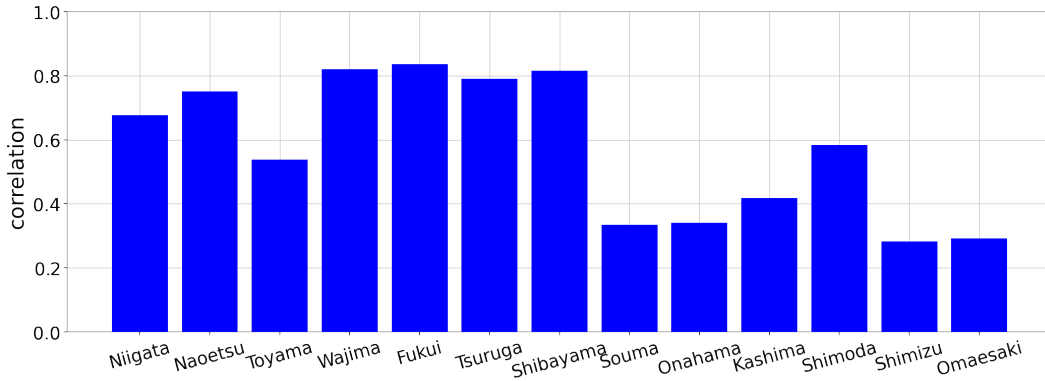


**Figure 9.** The correlation coefficient between the microseismic motion at the KAGRA site and the significant wave heights (SWH) at the 13 coasts in Japan, in 2020.

141 Here, we predict the microseismic motion at the KAGRA site using wave data  
 142 from 12 locations (other than Toyama Bay) in the NOWPHAS. In this study, the  
 143 ground velocity BLRMS  $v$  and SWH  $H_{1/3}$  are used with squared values to calculate  
 144 the energy. The SWH data between locations that are close to each other have a strong  
 145 positive correlation, as shown in Figure 8. To solve the degeneracy of the data, principal  
 146 component analysis (PCA) is applied to three areas of the ocean: the Sea of Japan side  
 147 (Niigata, Naoetsu, Wajima, Fukui, Tsuruga, and Shibayama), the eastern Pacific side  
 148 (Soma, Onahama, and Kashima), and the southern Pacific side (Shimoda, Shimizu, and  
 149 Omaesaki). Standardization of each squared SWH  $H_{1/3,j}^2(t)$  is performed to obtain the  
 150 mean 0 and standard deviation 1.

$$151 \quad x_j(t) = \frac{H_{1/3,j}^2(t) - \mu_j}{\sigma_j}, \quad (2)$$

152 where  $x_j(t)$  is the standardized wave data and  $\mu_j, \sigma_j$  are the mean and the standard  
 153 deviation of  $H_{1/3,j}^2(t)$  for the  $j$ -th location of the NOWPHAS site. The PCA (via

154 `scikit-learn 1.0.2` is performed for three areas (Sea of Japan side, eastern Pacific  
 155 side, and southern Pacific side) labeled by index  $i$ :

$$156 \quad PC_i(t) = \sum_j c_{ij} x_j(t), \quad (3)$$

157 where  $PC_i(t)$  is the first-principal component, and  $c_{ij}$  is its eigenvector for the  $i$ -th area.  
 158 The PCA parameter values are summarized in Table 1.

**Table 1.** Summary of the ocean wave data.  $\mu$  and  $\sigma$  represent the mean and standard deviation of the squared wave heights, respectively, while the remaining data show the PCA eigenvectors for three areas: the Sea of Japan side, the Eastern Pacific side, and the Southern Pacific side.

	$\mu$ [m <sup>2</sup> ]	$\sigma$ [m <sup>2</sup> ]	$c_{ij}$		
			sea of Japan	eastern Pacific	southern Pacific
Niigata	1.7	3.1	0.39	–	–
Naoetsu	1.8	3.1	0.42	–	–
Wajima	2.3	3.5	0.43	–	–
Fukui	2.3	3.9	0.42	–	–
Tsuruga	1.3	2.5	0.40	–	–
Shibayama	2.2	3.3	0.39	–	–
Soma	1.2	1.8	–	0.58	–
Onahama	1.5	2.1	–	0.58	–
Kashima	2.4	3.3	–	0.57	–
Shimoda	1.0	1.0	–	–	0.58
Shimizu	0.26	0.32	–	–	0.59
Omaesaki	0.91	1.09	–	–	0.57

159 These principal components  $PC_i(t)$  are difficult to treat in comparison to the  
 160 microseismic motion because they are dimensionless and include negative values.  
 161 Therefore, the weighted average of the squared SWH

$$162 \quad \bar{H}_i^2(t) = \sum_j w_{ij} H_{1/3,j}^2(t), \quad w_{ij} = \frac{c_{ij}/\sigma_j}{\sum_k c_{ik}/\sigma_k}, \quad (4)$$

163 provides a better representation of the wave levels for each ocean area. Figure 10 and  
 164 Figure 11 are the correlation plots and the correlation coefficients for the observed  
 165 microseismic motion  $v^2(t)$  and the wave levels of the three ocean areas  $\bar{H}_i^2(t)$ . There  
 166 was no strong correlation between the individual representative significant wave heights.  
 167 They also showed that waves on the Sea of Japan side strongly influence the ground  
 168 vibration values.

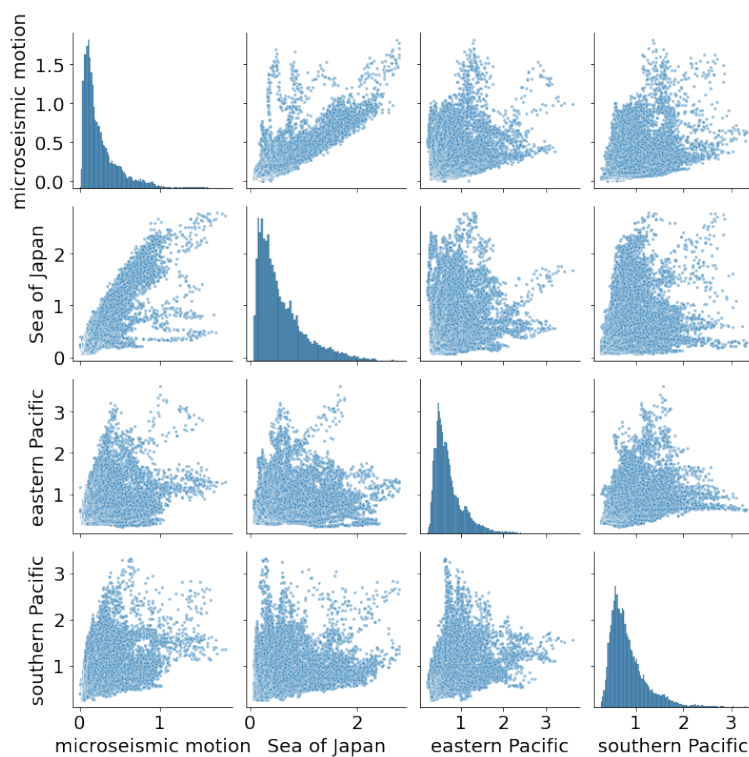


**Figure 10.** Scatter plot matrix of the observed microseismic motion at the KAGRA site and the representative wave levels for the sea of Japan, the eastern Pacific side, and the southern Pacific side.

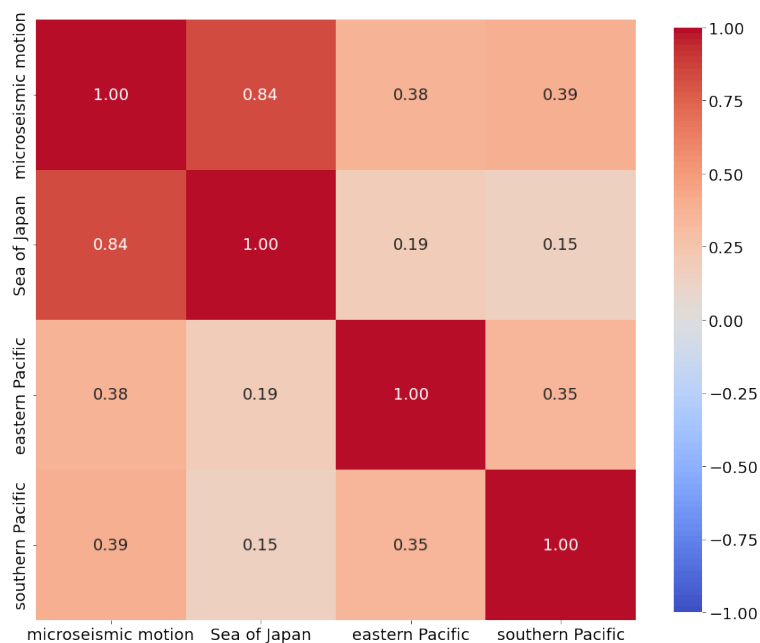


**Figure 11.** Correlation coefficient among the observed microseismic motion at the KAGRA site and the representative wave levels for the sea of Japan, the eastern Pacific side, and the southern Pacific side.

169

The prediction for the microseismic motion at the KAGRA site is written as follows:

170

$$v_{\text{pred}}^2(t) = \sum_i \alpha_i^2 \bar{H}_i^{2\beta_i}(t), \quad (5)$$

171

where  $\alpha_i$  and  $\beta_i$  are constants and are to be derived by fitting into the data with the non-

172

linear least squares method (via `scipy.optimize.curve_fit`). The results are shown

173

in Figure 12, where the black markers are the observed data and the red lines are the

174

predictions of the ground vibration BLRMS at the KAGRA site for one year. The values

175

of the fitting parameters are shown in Table 2. Almost good agreement between the

176

prediction and the observed data was observed except for the typhoon data not used in

177

the PCA and the fitting. The values of the index  $\beta_i$  are close to the  $b^{-1} \sim 1.5$  of Ferretti

178

*et al.* [26].

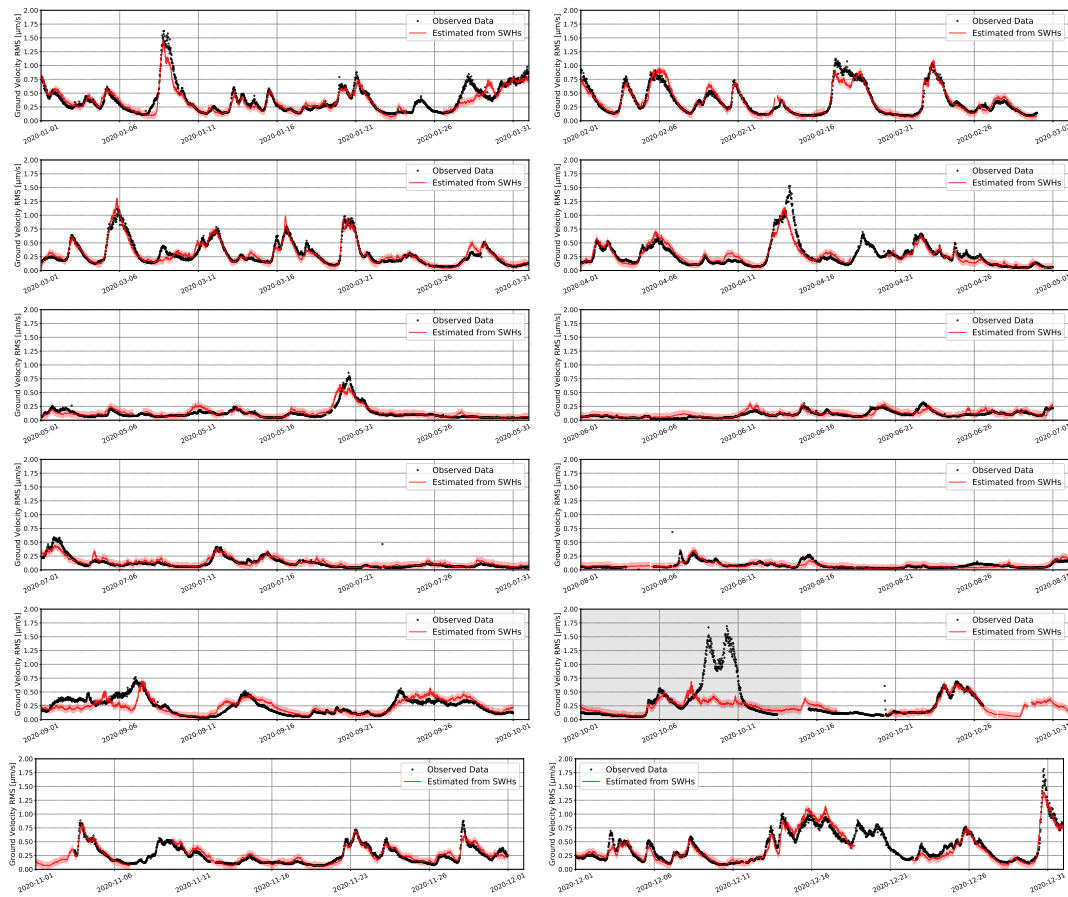


**Figure 12.** Comparison of the microseismic motion at the KAGRA site, between the observed data (black) and the prediction from the ocean waves (red, with the  $1\sigma$  error band). The typhoon period (gray hatched) is not used for the prediction.

**Table 2.** The results of the fitting parameters in Eq. (5).

	$\alpha_i$ [ $\mu\text{m/s/m}^{\beta_i}$ ]	$\beta_i$
Sea of Japan	$0.358 \pm 0.001$	$1.314 \pm 0.005$
Pacific east	$0.104 \pm 0.002$	$1.644 \pm 0.024$
Sacific south	$0.092 \pm 0.002$	$1.687 \pm 0.024$

179 To discuss the accuracy of this prediction, Figure 13 (left) shows a histogram of  
 180 the difference between the predicted and observed microseismic motion. It is almost  
 181 a Gaussian distribution and its mean and standard deviation are  $1.2 \times 10^{-3} \mu\text{m/s}$  and  
 182  $7.4 \times 10^{-2} \mu\text{m/s}$ , respectively. This standard deviation was used for the error band  
 183 in Figure 12. Figure 13 (right) shows a 2D histogram of the data points between  
 184 the predicted and observed microseismic motions, and good linearity was confirmed  
 185 for most parts. This is achieved owing to the index parameter  $\beta_i$ ; if it is not used  
 186 (corresponding to  $\beta_i = 1$ ), the prediction becomes systematically smaller when the ocean  
 187 waves are violent. The cluster distributes around  $v_{pred} \sim 0.3 \mu\text{m/s}$  and  $v_{obs} > 0.7 \mu\text{m/s}$   
 188 corresponding to the period that the typhoon was coming to Japan (during October  
 189 9–11). This is because an offshore typhoon directly shakes the seabed just below it, and  
 190 microseismic waves propagate to Japan even though the coasts are still not rough [27].

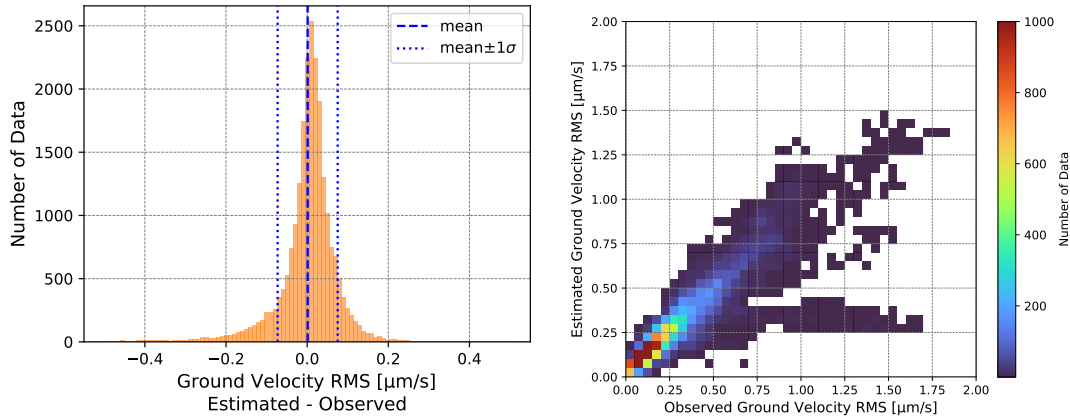


**Figure 13.** Left: Histogram of the difference between observed values and predicted values of the microseismic motion. Right: 2D histogram of the observed values and predicted values of the microseismic motion.

## 191 5. Conclusion and prospects

192 In this study, we investigated the properties of the microseismic motion at the KAGRA  
 193 site and the significant wave heights on the coasts of Japan measured and opened by  
 194 NOWPHAS for 2020. The degeneracy of the wave data was solved using a principal  
 195 component analysis, and the first-principal components of the three ocean regions were  
 196 extracted. Microseismic motion observed at the KAGRA site was almost predicted by

197 the combination of these components of the ocean waves within the standard deviation  
 198 of  $7 \times 10^{-2} \mu\text{m/s}$ .

199 In this paper, only the first principal components for each sea area are used, and  
 200 other principal components (which contain the local information) are not reflected.  
 201 Models that incorporate all information may provide better prediction accuracy. Other  
 202 ocean waves data, such as significant wave periods and wind direction, are also  
 203 important. Machine learning is a possible way to improve this analysis. To include  
 204 typhoon days, the development of special treatments is necessary, *e.g.* using the position  
 205 and magnitude of the typhoon.

206 A useful application of this study is *the microseismic forecast*. Future microseismic  
 207 motion can be forecasted by inputting wave information from commercial weather  
 208 forecasts into our equation. Figure 14 shows an example of a microseismic forecast using  
 209 a 1-week weather forecast on the website [tenki.com](http://tenki.com) provided by Bellsystem24 Inc [28].  
 210 The blue line represents the forecast with the error band of microseismic motion at the  
 211 KAGRA site. The vertical black dotted line represents the current time, and the right  
 212 and left-hand sides represent the future and past, respectively. The horizontal dotted  
 213 lines (red and yellow) correspond to the benchmark microseismic levels discussed in  
 214 Section 2. The historical data is overlaid with BLRMS of the actual measured values  
 215 for comparison. This plot is automatically updated and shown on a website (internal  
 216 page) and contributes to commissioning works at the KAGRA observatory, especially  
 217 for its scheduling.

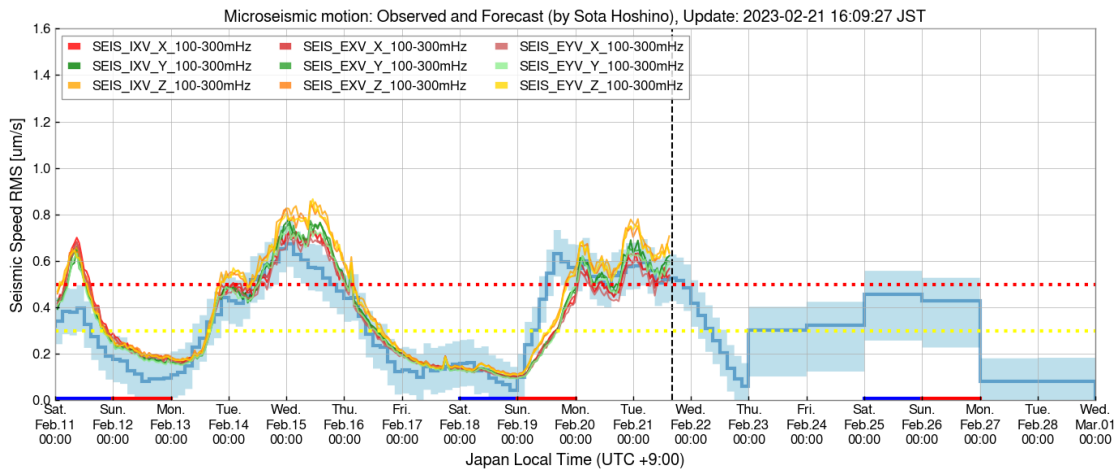


**Figure 14.** An example of the microseismic forecast graph. The black line shows the current date, in this case, 2023-05-18 11:09 (JST). The right and left sides of it are the future and past, respectively. The horizontal dotted lines (red and yellow) correspond to the benchmark microseismic level discussed in Sec. 2, red is  $0.5 \mu\text{m/s}$ , and yellow is  $0.3 \mu\text{m/s}$ . The historical data is overlaid with BLRMS of the actual measured triaxial ground vibrations from the three seismometers located at the KAGRA site for comparison.

218 **Acknowledgement**

219 This research has made use of data, software, and web tools obtained or developed  
220 by the KAGRA Collaboration, especially the administrators of the digital system, and  
221 managers of the KAGRA site. The NOWPHAS data is provided by the Port and  
222 Harbor Bureau, Ministry of Land, Infrastructure, Transport and Tourism, Japan, and  
223 the weather forecast data is provided by Bellsystem24 Inc.

224 The KAGRA project is supported by MEXT, JSPS Leading-edge Research  
225 Infrastructure Program, JSPS Grant-in-Aid for Specially Promoted Research 26000005,  
226 JSPS Grant-in-Aid for Scientific Research on Innovative Areas 2905: JP17H06358,  
227 JP17H06361 and JP17H06364, JSPS Core-to-Core Program A. Advanced Research  
228 Networks, JSPS Grant-in-Aid for Scientific Research (S) 17H06133 and 20H05639,  
229 JSPS Grant-in-Aid for Transformative Research Areas (A) 20A203: JP20H05854,  
230 the joint research program of the Institute for Cosmic Ray Research, University of  
231 Tokyo, National Research Foundation (NRF), Computing Infrastructure Project of  
232 Global Science experimental Data hub Center (GSDC) at KISTI, Korea Astronomy  
233 and Space Science Institute (KASI), and Ministry of Science and ICT (MSIT) in  
234 Korea, Academia Sinica (AS), AS Grid Center (ASGC) and the National Science  
235 and Technology Council (NSTC) in Taiwan under grants including the Rising Star  
236 Program and Science Vanguard Research Program, Advanced Technology Center (ATC)  
237 of NAOJ, and Mechanical Engineering Center of KEK. Especially this work was founded  
238 by JSPS Grant-in-Aid for JSPS Fellows 19J01299 and the Joint Research Program of  
239 the Institute for Cosmic Ray Research (ICRR) University of Tokyo 2020-G07, 2020-G12,  
240 2020-G21, 2021-G07, 2021-G09, 2021-G10, 2022-G07, 2022-G12, 2022-G21.

241 We would like to thank Editage ([www.editage.com](http://www.editage.com)) for English language editing.

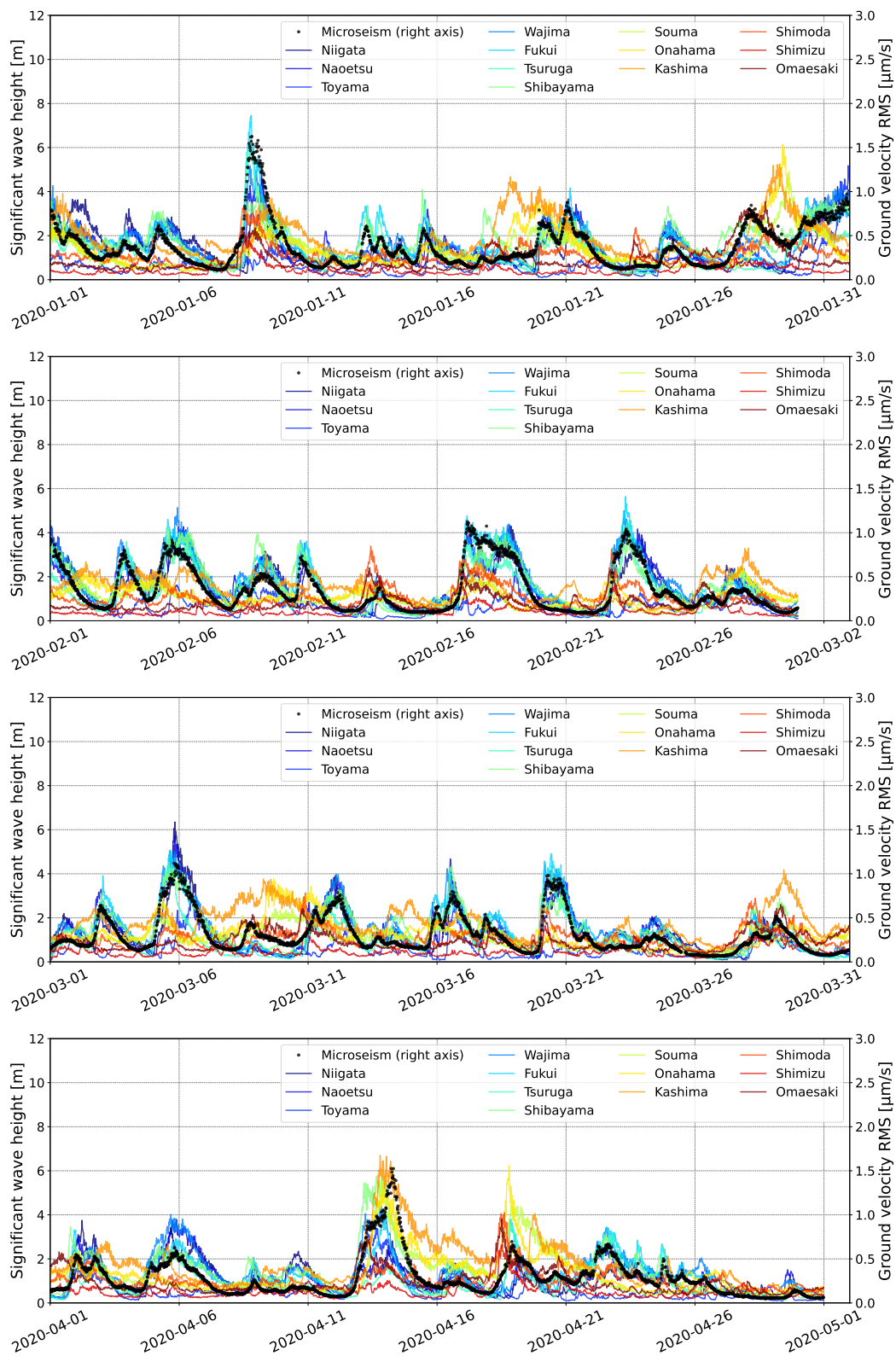
## Appendix A. One year data of the SWH and the microseismic motion

Appendix A contains SWH time series data for the full year 2020 that were not shown in Figure 5. In addition, this figure overlays the BLRMS of the KAGRA seismometer data.

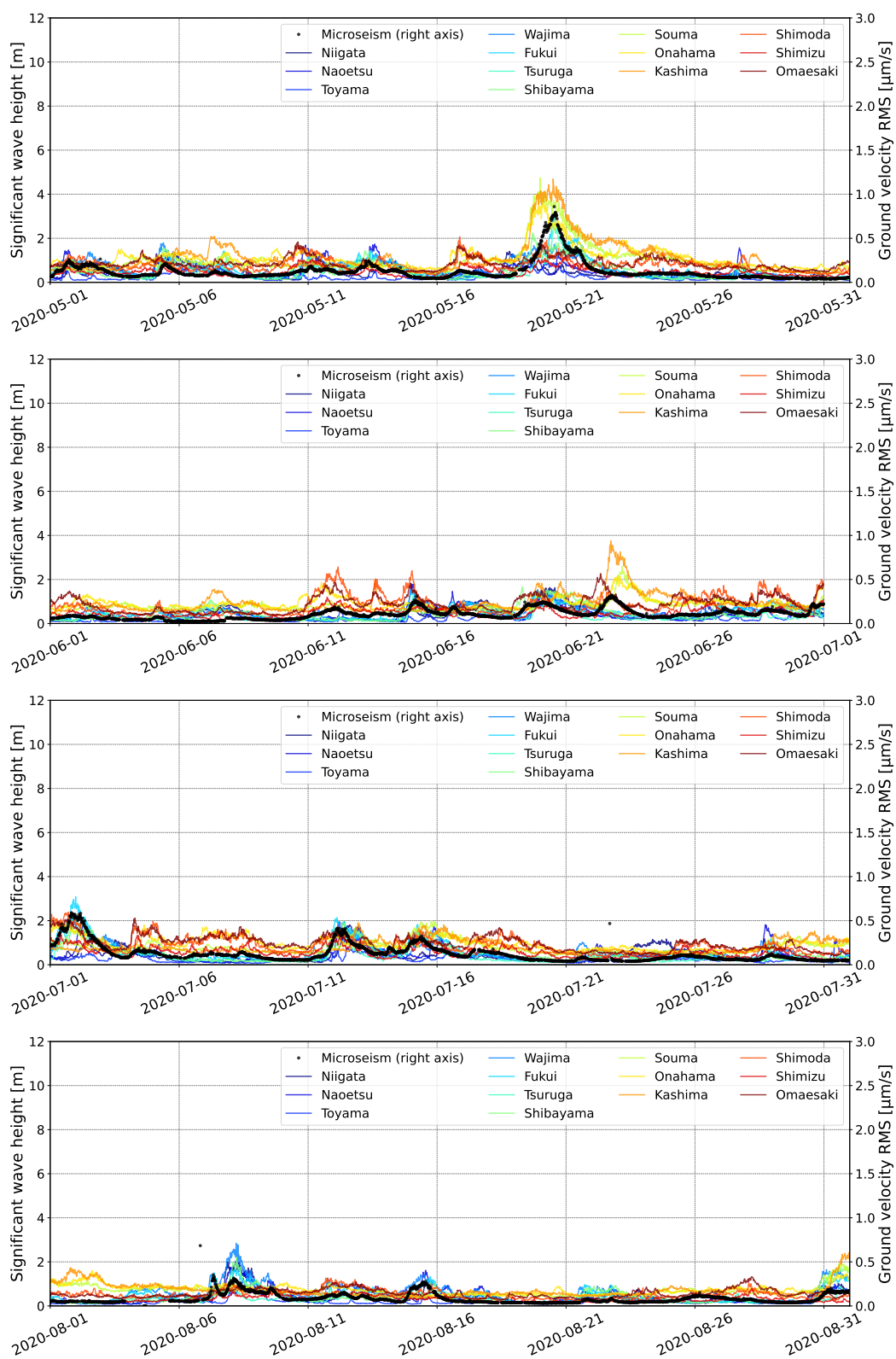
## Reference

- [1] LIGO Scientific Collaboration 2014 Advanced LIGO Class. Quantum Grav. 32 074001
- [2] B. P. Abbott et al.(LIGO Scientific Collaboration and Virgo Collaboration) 2016 GW150914: The Advanced LIGO Detectors in the Era of First Discoveries Phys. Rev. Lett. 116, 131103
- [3] F. Acernese et al. 2014 Advanced Virgo: a second-generation interferometric gravitational wave detector Class. Quantum Grav. 32 (2015) 024001
- [4] B. P. Abbott et al. (LIGO Scientific Collaboration and Virgo Collaboration) 2017 A Three-Detector Observation of Gravitational Waves from a Binary Black Hole Coalescence Phys. Rev. Lett. 119, 141101
- [5] B. P. Abbott et al. (LIGO Scientific Collaboration and Virgo Collaboration) 2017 GW170817: Observation of Gravitational Waves from a Binary Neutron Star Inspiral Phys. Rev. Lett. 119, 161101
- [6] Akutsu T et al (KAGRA Collaboration) 2020 Overview of KAGRA: Detector design and construction history Prog. Theor. Exp. Phys. ptaa125
- [7] T. Akutsu et al. (KAGRA Collaboration) 2020 Application of the independent component analysis to the iKAGRA data Progress of Theoretical and Experimental Physics, Volume 2020, Issue 5, May 2020, 053F01
- [8] T. Akutsu et al. 2019 First cryogenic test operation of underground km-scale gravitational-wave observatory KAGRA Class. Quantum Grav. 36 165008
- [9] T. Akutsu et al. 2018 Construction of KAGRA: an underground gravitational-wave observatory Progress of Theoretical and Experimental Physics, Volume 2018, Issue 1, January 2018, 013F01
- [10] T. Akutsu et al. 2019 First cryogenic test operation of underground km-scale gravitational-wave observatory KAGRA Class. Quantum Grav. 36 165008
- [11] the KAGRA collaboration Alexander Novikov, Pierre P etroff, Christophe Royon, and K Kokeyama 2020 Observing the Universe from Underground Gravitational Wave Telescope KAGRA 3rd World Summit on Exploring the Dark Side of the Universe (EDSU2020) (Guadeloupe Islands March 9–13 2020) pp 41–8 <http://hdl.handle.net/1808/30804>
- [12] H. Abe et al. 2022 The Current Status and Future Prospects of KAGRA, the Large-Scale Cryogenic Gravitational Wave Telescope Built in the Kamioka Underground Galaxies 2022, 10(3), 63; <https://doi.org/10.3390/galaxies10030063>
- [13] Y. Fujikawa 2021 Master thesis of Fujikawa(Japanese)
- [14] M. S. Longuet-Higgins 1950 A theory of the origin of microseisms Royal Society 27 September 1950 Volume 243Issue 857
- [15] K. Hasselmann 1963 A statistical analysis of the generation of microseisms Rev. Geophys Volume1, Issue2 May 1963 Pages 177-210
- [16] T. Tanimoto 2007 Excitation of normal modes by non-linear interaction of ocean waves Geophysical Journal International, Volume 168, Issue 2, February 2007, Pages 571–582
- [17] T. Tanimoto. 2007 Excitation of microseisms Geophysical Research Letters Volume34, Issue5 March 2007
- [18] P. D. Bromirski et al. 1999 Ocean wave height determined from inland seismometer data: Implications for investigating wave climate changes in the NE Pacific JGR Oceans Volume104, IssueC9 15 September 1999 Pages 20753-20766

*Evaluation of the microseismic motion at the KAGRA site based on the ocean wave data*16



*Evaluation of the microseismic motion at the KAGRA site based on the ocean wave data* 17



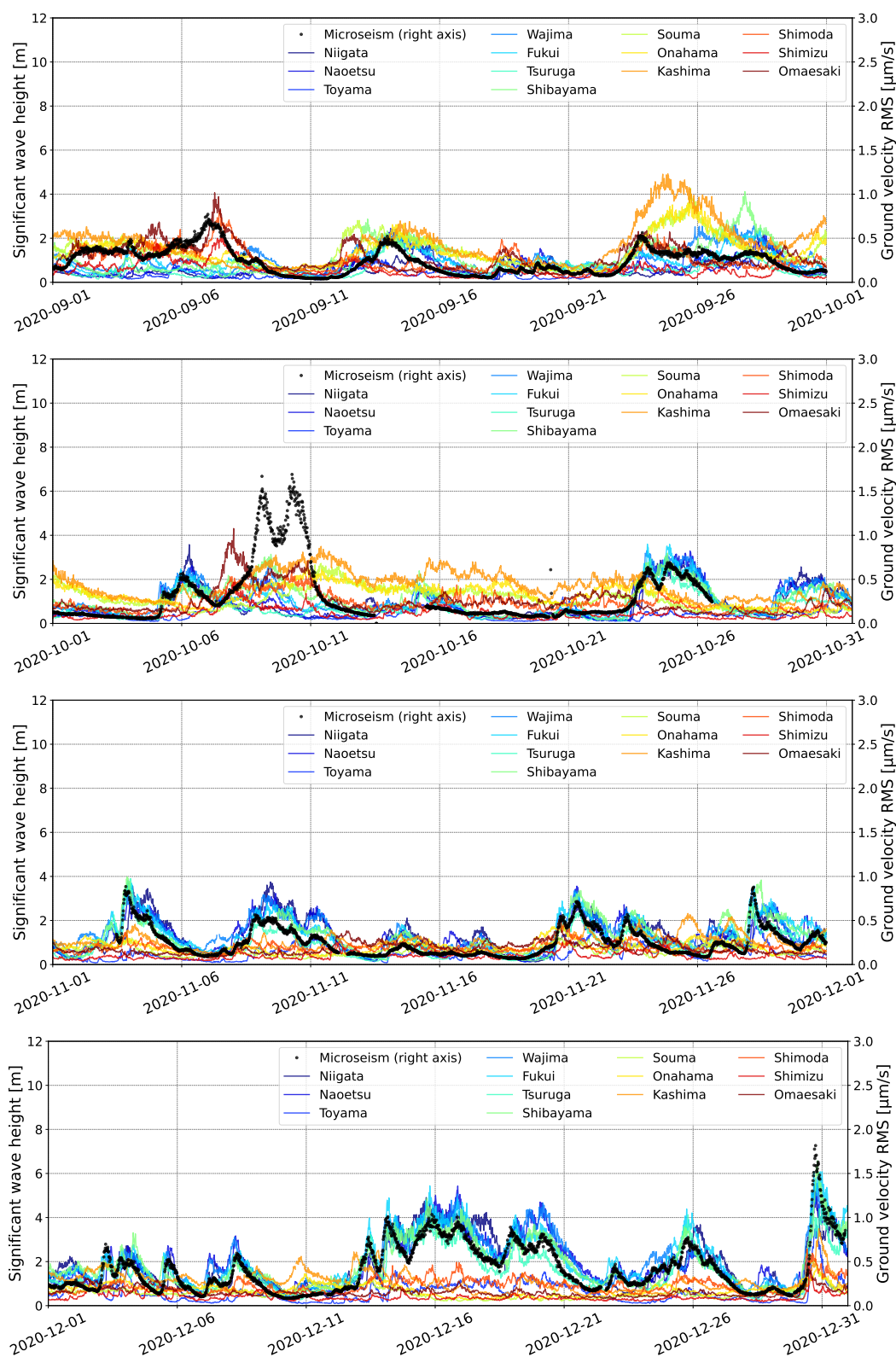


**Figure A1.** The time series data of the SWH in NOWPHAS and the microseismic motion at the KAGRA site, partially shown in Figure 5, are shown here through the full year 2020.

- 288 [19] F. Badaracco et al. 2021 KAGRA underground environment and lessons for the Einstein Telescope  
289 Phys. Rev. D 104, 042006
- 290 [20] S. Miyoki Current status of KAGRA 2020 Ground-based and Airborne Telescopes VIII. SPIE,  
291 2020, Vol. 11445, pp. 192–204. doi:10.1117/12.2560824.
- 292 [21] J. R. Peterson 1993 Observations and modeling of seismic background noise U.S. Geological Survey  
293 <https://doi.org/10.3133/ofr93322>
- 294 [22] T. Washimi et al. 2022 Response of the underground environment of the KAGRA observatory  
295 against the air-pressure disturbance from the Tonga volcano eruption on January 15th, 2022  
296 Progress of Theoretical and Experimental Physics, Volume 2022, Issue 11, November 2022,  
297 113H02
- 298 [23] Alessandro et al. 2021 Local Hurst Exponent Computation of Data from Triaxial Seismometers  
299 Monitoring KAGRA Pure Appl. Geophys. 178, 3461–3470
- 300 [24] The Nationwide Ocean Wave information network for Ports and HARbourS, NOWPHAS Web site:  
301 [https://www.mlit.go.jp/kowan/nowphas/index\\_eng.html](https://www.mlit.go.jp/kowan/nowphas/index_eng.html)
- 302 [25] Y Hida et al. Verification of Simulated Waves for Statistical Aspects in Zero-Cross Methods
- 303 [26] G. Ferretti et al. 2013 On microseisms recorded near the Ligurian coast (Italy) and their  
304 relationship with sea wave height Geophysical Journal International, Volume 194, Issue 1, July  
305 2013, Pages 524–533
- 306 [27] Jian Zhang, Peter Gerstoft, and Peter D. Bromirski 2010 Pelagic and coastal sources of P-wave  
307 microseisms: Generation under tropical cyclones Geophysical Research Letters Volume 37, Issue  
308 15
- 309 [28] Otenki.com Bellsystem24, Inc. Web site: <https://hp.otenki.com/>